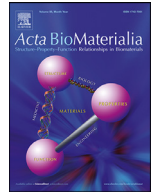




ELSEVIER

Contents lists available at ScienceDirect

Acta Biomaterialia

journal homepage: www.elsevier.com/locate/actbio

Full length article

Jackfruit: Composition, structure, and progressive collapsibility in the largest fruit on the Earth for impact resistance

Benjamin S. Lazarus^{a,*}, Victor Leung^b, Rachel K. Luu^{b,c}, Matthew T. Wong^d,
Samuel Ruiz-Pérez^e, Willams T. Barbosa^f, Wendell B. Almeida Bezerra^g,
Josiane D.V. Barbosa^f, Marc A. Meyers^{a,b,d}

^a Materials Science and Engineering Program, University of California San Diego, USA

^b Department of Mechanical and Aerospace Engineering, University of California San Diego, USA

^c Department of Materials Science and Engineering, Massachusetts Institute of Technology, USA

^d Department of Nanoengineering, University of California San Diego, USA

^e Facultad de Ciencias, Universidad Nacional Autónoma de México, Mexico City, Mexico

^f Department of Materials, University Center SENAI CIMATEC, Salvador, Brazil

^g Department of Materials Science, Military Institute of Engineering-IME, Rio de Janeiro 22290270, Brazil

ARTICLE INFO

Article history:

Received 30 January 2023

Revised 17 April 2023

Accepted 26 April 2023

Available online xxx

Keywords:

Impact resistance

Bioinspiration

3D printing

Collapsibility

Chemical and mechanical characterization

ABSTRACT

The jackfruit is the largest fruit on the Earth, reaching upwards of 35 kg and falling from heights of 25 m. To survive such high energy impacts, it has evolved a unique layered configuration with a thorny exterior and porous tubular underlayer. During compression, these layers exhibit a progressive collapse mechanism where the tubules are first to deform, followed by the thorny exterior, and finally the mesocarp layer in between. The thorns are composed of lignified bundles which run longitudinally from the base of the thorn to the tip and are embedded in softer parenchymal cells, forming a fiber reinforced composite. The mesocarp contains more lignin than any of the other layers while the core appears to contain more pectin giving rise to variations in compressive and viscoelastic properties between the layers. The surface thorns provide a compelling impact-resistant feature for bioinspiration, with a cellular structure that can withstand large deformation without failing and wavy surface features which densify during compression without fracturing. Even the conical shape of the thorns is valuable, presenting a gradually increasing surface area during axial collapse. A simplified model of this mechanism is put forward to describe the force response of these features. The thorns also distribute damage laterally during impact and deflect cracks along their interstitial valleys. These phenomena were observed in 3D printed, jackfruit-inspired designs which performed markedly better than control prints with the same mass.

Statement of significance

Many biological materials have evolved remarkable structures that enhance their mechanical performance and serve as sources of inspiration for engineers. Plants are often overlooked in this regard yet certain botanical components, like nuts and fruit, have shown incredible potential as blueprints for improved impact resistant designs. The jackfruit is the largest fruit on Earth and generates significant falling impact energies. Here, we explore the jackfruit's structure and its mechanical capabilities for the first time. The progressive failure imparted by its multilayered design and the unique collapse mode of the surface thorns are identified as key mechanisms for improving the fruit's impact resistance. 3D printing is used to show that these structure-property benefits can be successfully transferred to engineering materials.

© 2023 The Authors. Published by Elsevier Ltd on behalf of Acta Materialia Inc.

This is an open access article under the CC BY-NC-ND license (<http://creativecommons.org/licenses/by-nc-nd/4.0/>)

* Corresponding author at: Materials Science and Engineering Program, University of California San Diego.

E-mail address: bslazaru@eng.ucsd.edu (B.S. Lazarus).

<https://doi.org/10.1016/j.actbio.2023.04.040>

1742-7061/© 2023 The Authors. Published by Elsevier Ltd on behalf of Acta Materialia Inc. This is an open access article under the CC BY-NC-ND license (<http://creativecommons.org/licenses/by-nc-nd/4.0/>)

1. Introduction

Biological materials contain a wide variety of hierarchical design strategies that allow them to withstand the dynamic loading

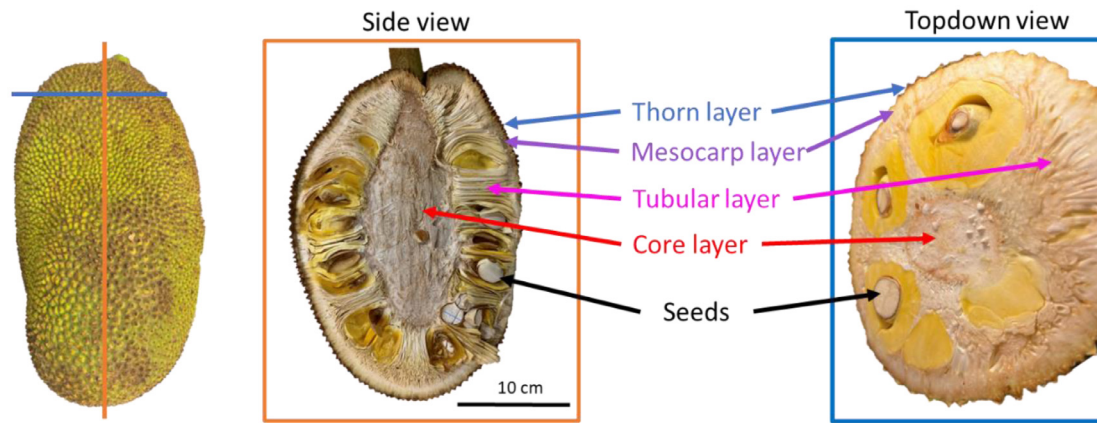


Fig. 1. A visualization of the jackfruit's interior showing vertical and horizontal cross-sections.

conditions imposed by their environment. To learn from these impressive systems, researchers have explored the mechanical properties of an array of materials generated by organisms within the animal kingdom, ranging from airborne creatures like woodpeckers [1] and pelicans [2] to animals that thrive deep under the sea such as whales [3] and conches [4]. However plant-based systems generally receive less attention than their Animalia counterparts yet have developed unique structural motifs with different constituent materials; to resist impact events. The trunks of certain trees, for example, contain a remarkable number of mesoscale features such as porosity and lignified reinforcing elements whose arrangement dictates their response to impact [5].

Researchers have also evaluated the impact resistance of nuts and fruits of certain plants which need to withstand falling impacts or offer protection from predators. One of the most widely studied fruits is the pomelo which contains a thick porous mesocarp whose primary function is to protect the seeds in the fruit's interior. The mesocarp of the pomelo is an open cell foam-like structure composed of fluid-filled struts. This structure imbues the fruit with several energy dissipation mechanisms during compression. The open cell-structure, which can reach a porosity of 80%, absorbs strain energy during impact. In fact, Seidel et al. [6] determined that the mesocarp only begins to densify at strains of ~55%, emphasizing the extreme collapsibility of this configuration. These results were verified by compressive *in-situ* computed tomography (CT) experiments [7]. The pomelo utilizes numerous structural gradients in the mesocarp to enhance its collapsibility, including gradients in porosity, cell size, and stiffness between adjoining features such as the stiffer, branching, lignified vascular bundles.

The pomelo peel also cleverly utilizes branch length of the vascular bundles; shorter branches are more resistant to buckling and bending. By varying the branch frequency in different regions of the peel, the fruit is able to tune the onset of densification by location [8]. Several groups have also observed, modeled, and replicated the viscoelastic and damping properties that arise from the strut structure, leading to bioinspired materials with high energy dissipation under compression [9–13].

Other nut [14] and fruit systems such as the macadamia nut [6,9,15], Brazil nut [16–18], coconut [19–22], cocoyol fruit [23], walnut [24,25], and apple [26] have been explored as a means of obtaining inspiration from nature. Recently, Ha et al. [27] turned to the durian as a subject for bioinspiration to create impact resistant packaging designed to protect goods during transport. The durian's most striking feature are the thorns that cover its surface. Just beneath the thorns is a fleshy mesocarp layer which transitions into the endocarp and ultimately the nutritious flesh and seeds above the core of the fruit. Ha et al. [27] performed uniaxial compressive tests on the thorny and the mesocarp layers beneath and found

that the thorny layer has a specific energy absorption nearly twice that of the mesocarp layer. They observed that when a small portion of the surface was impacted, thorns at the center of the impact buckle and the reinforcing fibers within the thorns delaminate, while thorns near the exterior of the sample bend and compress fibers at their bases. They point out that these unique failure and energy absorptive mechanisms may provide a novel source of bioinspiration for impact resistant materials.

The jackfruit is similar to the durian but with several key differences. The mass of a durian fruit is ~1.5 kg and it grows approximately 12 m up in trees corresponding to a falling energy of ~176 J. Jackfruit, on the other hand, are the largest fruit on the Earth reaching 35 kg in weight, although record-holding jackfruit weighing upwards of 50 kg have been reported. They grow along the branches and trunks of trees which can reach 25 m in height [28,29]. Given these metrics, falling jackfruit can experience impact energies of >8.5 kJ, approximately 50 times that of durian. In order to accommodate such massive impacts, the jackfruit has incorporated an extra layer of cushioning between the seeds and the endocarp. This region is composed of aligned tubules that run from the fruit's stiff core to the underside of the mesocarp where they densely before finally attaching to the base of an individual surface thorn (Fig. 1). Ha et al. [27] note that the thorns of the durian have a high aspect ratio, making them more susceptible to bending under impact. The jackfruit, on the other hand, has thorns that are shorter and wider (Fig. 1).

The jackfruit has numerous architectures and biomechanical functions that, to the authors' knowledge, have never heretofore been explored from an engineering perspective. As such, this biological system is a ripe candidate for bioinspiration. This study offers insight into the unique ways the jackfruit mitigates damage during impact events and provides blueprints for how engineered materials can utilize jackfruit-inspired design motifs for improved impact resistance. For the former, the composition of each layer of the jackfruit and its underlying microstructure is explored for the first time. Like many biological systems, these traits are finely tuned for the functionality of each component and here they are connected to the compressibility, viscoelasticity, and deformation modes of the jackfruit's hierarchical structure. In the case of the latter, numerous mechanisms are identified that improve the survivability of the jackfruit such as the progressive failure of the fruit's layered configuration, damage control of the thorny surface structure, and the gradually increasing resistance to axial loading afforded by the conical thorn shape. Here a model is introduced to describe the effect of the thorns macroscale shape during compression and 3D printed jackfruit-inspired designs show that the thorn can successfully reduce penetrative damage in engineered systems.

2. Methods and materials

2.1. Sample acquisition

Whole jackfruits were acquired from 99 Ranch market in San Diego. Impact resistance in fruit may seem counterintuitive since these energy-rich capsules are often meant to act as vehicles for spreading an organism's offspring either through predation or by releasing seeds upon separation from the plant. Our hypothesis is that the impact resistance in jackfruit is meant to allow immature fruit to withstand falling damage and continue to ripen on the forest floor. Simple free fall tests, where jackfruits of different ages were dropped from a height of 7.6 m onto a concrete slab, confirmed this; while older, ripe jackfruit ruptured, equally-sized unripe jackfruit withstood the impact, even surviving six sequential drops. Concordantly, slightly underripe jackfruit, which were just beginning to transition from green to brown, were purchased for testing.

2.2. Microcomputed tomography (microCT)

High resolution 3-D images were acquired by microcomputed tomography (Skyscan 1076, Bruker, Kontich, Belgium) at 35 μ m³ voxel resolution. The sample was wrapped in plastic wrap and enclosed in a sandwich-sized ziploc bag. The bag was wedged between styrofoam blocks, taped together, and then placed inside a plastic jar, and further secured using additional styrofoam blocks to minimize shifting during scanning. It was scanned as an oversized and wide (x2) scan in three fields encompassing its entirety using imaging parameters of 60 kVp, 16 7 μ A, Al 0.5 mm filter, 180 degrees, 0.5 degree step rotations, and 3 frame averaging. Scans were reconstructed (Smoothing = 1, Ring Artifact = 6, Beam Hardening = 40%, Gaussian kernel, Dynamic Range = -0.010 to 0.020, NRecon, Bruker, Kontich, Belgium) with auto x/y and z alignment and fusion to stitch the three sets together. An image quality check was performed by positioning the cursor at the center of the sample (DataViewer, Bruker, Kontich, Belgium) in the skin, skin/fruit interface, and fruit; three 2-D orthogonal views were checked for quality (presence and clarity of structural features) and absence of noise or imaging artifacts, and then recorded for presentation. The results were processed with Fiji (U. S. National Institutes of Health, Bethesda, Maryland, USA) [30] and 3D plugins [31,32].

2.3. Scanning electron microscopy (SEM)

Samples were extracted from each layer of the jackfruit and imaged using an FEI Apreo FESEM (Thermo Fisher Scientific, Waltham, Massachusetts, USA) after being sputter coated (Emitech K575X, Quorum Technologies Ltd, East Sussex, United Kingdom) with iridium for eight seconds. Measurements were taken using Fiji/ImageJ (U. S. National Institutes of Health, Bethesda, Maryland, USA) [30]. To visualize its compressive behavior, sputter coated thorn samples were mounted between two screw driven compression plates using carbon tape. A small section of the thorns' skin was cut and peeled back to reveal the cellular structure beneath. The screw was then turned to compress the sample to specific strains and images were taken of the structural changes that occurred both on the surface of the thorn as well as in the underlying region. The spacing of the surface wrinkles were measured ($n = 150$) at four increments of engineering strain (0%, 36%, 54%, and 72%) using Fiji [30].

2.4. Optical microscopy

Thin slices of each layer were prepared by hand using a scalpel and stained with Toluidine Blue O (Sigma-Aldrich, St. Louis, USA)

following the procedure laid out in [33]. Images of the stained samples were taken using an Olympus AX70 optical microscope (Olympus, Tokyo, Japan).

2.5. Thermogravimetric analysis (TGA)

Thermogravimetric analysis was performed on samples from each layer and were heated from 25°C to 700°C at a ramp rate of 10°C/min. Samples were dried in an oven at 105°C for 24 hours immediately before testing to remove as much moisture as possible.

2.6. Compression, stress relaxation, and compact tension

Quasi-static compressive tests were performed on samples taken from the different regions of the jackfruit at three different strain-rates (10⁰ s⁻¹, 10⁻¹ s⁻¹, and 10⁻² s⁻¹). To maintain sample homogeneity, 5×5×5mm³ samples were prepared and tested using an Instron 3342 universal testing system (Instron, High Wycombe, United Kingdom) equipped with a 500 N load cell. Owing to their small size, whole individual thorns were removed from the jackfruit exterior and tested. For stress-relaxation tests, samples were compressed to 90% of their original height at a strain rate of 10⁻¹ s⁻¹ and then allowed to relax for 900 s. The resulting curves were fitted to a three-element Maxwell-Weichert model using a Prony series. This model involves a spring in parallel with three Maxwell elements (each consisting of a spring and dashpot in series). Compact tension tests were also performed on two-layer samples which included the thorny exterior and mesocarp. These samples were fabricated to adhere to the Plastic ASTM D5045 – 14 standard ($W = 40$ mm). Tests were performed at three different cross-head speeds of 10 mm/min, 60 mm/min, and 120 mm/min.

2.7. Digital image correlation (DIC)

Samples were speckled using a Speckler Pattern Application Kit (Correlated Solution, Irmo, USA). A random speckle pattern with a dot size of 0.33 mm was imprinted on the surface of samples. Videos recorded during the tests and then still images were extracted. These stills were used to create strain maps during the tests using the open-source 2D-DIC Matlab software, Ncorr (Georgia Institute of Technology, Atlanta, USA).

2.8. Gas gun impact testing

Gas gun testing was performed using a modified paintball gun mounted to a frame 30 cm above the sample which was placed on a metal surface. Rubber-coated steel balls 17.3 mm in diameter with a mass of 6.92 grams were used as projectiles. The paintball gun was connected to an Arduino microcontroller in order to fire the round. The microcontroller is used to activate a servo motor that in turn triggers the paintball gun. To trigger the high-speed camera, a laser trigger was set up in order to detect when the round was fired. This consists of a Thorlabs (Newton, NJ, USA) CPS532 laser that is detected with a Thorlabs PDA10A2 Si Amplified Fixed Gain Detector. The output signal can be viewed through a Tektronix DPO 2014 oscilloscope. The oscilloscope is connected to a Tektronix AFG3022C function generator. Once the laser beam is broken, it is registered by the photodetector and displayed on the oscilloscope. This then causes the function generator to send a signal to trigger the i-Speed 716 high speed camera. Videos were recorded at frames per second between 40,000 and 75,000.

A total of 13 samples were prepared, each with two samples containing the following layers: mesocarp and tubules, mesocarp and thorns, mesocarp only, thin mesocarp and tubules. Five samples were prepared consisting of thorns, mesocarp, and tubules,

with all but one sample having speckles for digital image correlation (DIC). The samples were cut to have a cross-section of 3 cm × 3 cm, with the height dependent on which layers were being tested. Samples were tested within three hours of cutting.

2.9. Free fall tests

To confirm that the jackfruit is intended to withstand freefall impacts rather than failing as a seed dispersal mechanism, jackfruits were dropped onto a concrete slab from 7.6 m high. Video footage was used to capture the deflection distance of the fruit's surface to estimate the maximum impact force experienced during the fall.

2.10. Bioinspired samples

Bioinspired samples were designed based on cross-sectional images of the jackfruit. Traces of the thorn and tubule dimensions were extruded and then combined using Fusion 360 CAD software (Autodesk, San Rafael, USA). Four different types of jackfruit-inspired designs were printed; samples modeled after all three of the outer layers of the jackfruit (thorns, mesocarp, and tubules) as well as samples with just the thorn and mesocarp layers, mesocarp and tubular layers, and samples of just tubules. Bioinspired samples were printed out of polyethylene terephthalate glycol (PETG) using an Ender 3 Pro (Creality, Shenzhen, China) using a 0.4 mm diameter nozzle. Several different infills (of 10%, 15%, and 20%) were tested all of which contained a cubic infill pattern with a print direction of 45 degrees. Prints were fabricated at a print temperature of 225°C onto a build plate heated to 85°C. The jackfruit-inspired samples were compared with featureless rectangular samples of the same mass.

2.11. Statistical analysis

The Prony series fit was carried out using an evolutionary optimization algorithm to minimize the residual sum squares of the

fitted curve by adjusting the input coefficients. The presented compression and compact tension data curves are averages with the standard deviation range at any given strain represented by the shaded area. The energy absorbed during compact tension tests is reported as an average with error bars representing the standard deviation of each dataset.

3. Results and discussion

3.1. Structure and composition

For the purpose of this study, the jackfruit was divided into four regions. From exterior to interior, these regions are the thorny surface exocarp, the mesocarp, the tubular region which contains the fruit's seeds, and the core of the fruit. The surface thorns were measured ($N = 16$) to have an average height (H) of $4.4 \text{ mm} \pm 1.5 \text{ mm}$, with a base width (W) of $4.6 \text{ mm} \pm 1.6 \text{ mm}$ and an inclination angle of $57.1^\circ \pm 3.2^\circ$ (H and W in Fig. 2A). While there was significant variation in the height and base dimensions for different thorns, the inclination angle was relatively consistent. Measuring the thorns by hand ($N = 30$) revealed an average tip diameter of about $1.57 \text{ mm} \pm 0.19 \text{ mm}$ and a polygonal base area of $33.21 \text{ mm}^2 \pm 4.98 \text{ mm}^2$. 2D hexagons are one of the most efficient shapes for two-dimensional packing [34] and they are ideal for having a high density of thorn tips covering the surface contours of the irregular surface of the fruit. Using computed tomography scans of the fruit's interior, the porosity of the tubular region was found to be approximately 56%. Individual hollow tubules ($N = 25$) were observed to be elliptical in cross-section with an average aspect ratio of 2.07 ± 0.48 . Average major and minor axes dimensions of $3469 \mu\text{m} \pm 571 \mu\text{m}$ and $1679 \mu\text{m} \pm 409 \mu\text{m}$, respectively, and wall thickness of $691 \mu\text{m} \pm 161 \mu\text{m}$. An example of these measurements can be seen in Fig. 2B, which shows a transverse slice of the jackfruit's tubule layer. Figs. 2C-E show 3D renderings of the jackfruit's different layers, except the core. From segmentation of the microCT

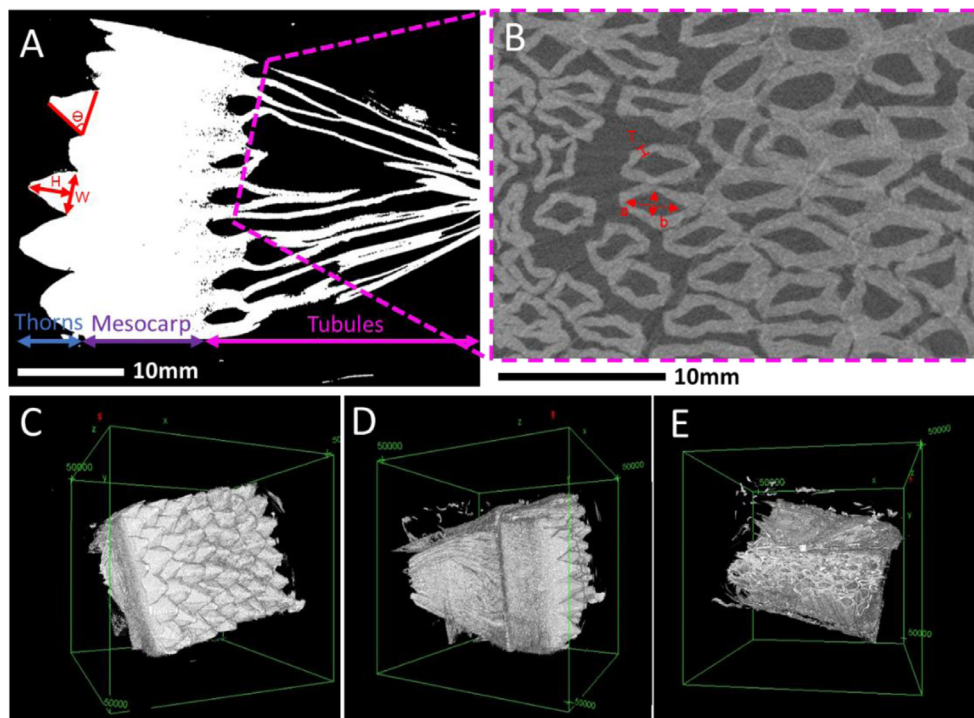


Fig. 2. Microcomputed tomography scans showing A.) a through-thickness cross-section of the thorn, mesocarp and tubular layer, B.) a cross-section of the tubular region, and C-E.) 3D renderings of the jackfruit's outer three layers. Each length of the green box is 50 mm.

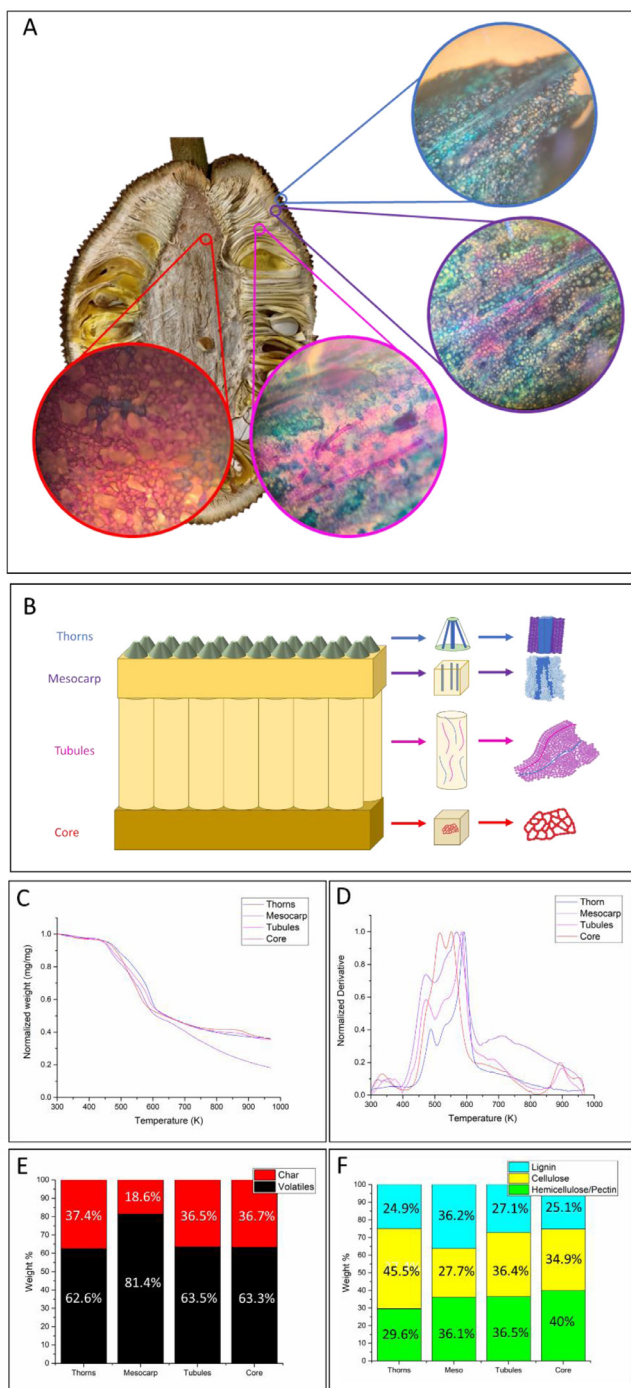


Fig. 3. The composition of the jackfruit is different in each layer. A.) Optical micrographs showing the results of O Tolidine blue staining from each layer. B.) Schematic illustration of the structure and arrangement of lignified fiber bundles and cells in the four layers. C.) Normalized TGA curve and D.) normalized DTG curve of the different layers. E.) Bar chart showing the volatile and residual char percentages for each layer and F.) Estimates of the composition of each layer based on the DTG curves.

results, it was determined that the tubule walls occupy approximately 43.9% of the cross-sectional area in the tubule region.

Toluidine Blue O is a polychromatic stain that can be used to differentiate plant tissues by preferentially binding with anionic groups in the cell wall. The result is a multicolored sample that gives insight into local composition. Fig. 3A shows microscopy images from each layer of the jackfruit. In the thorns, the reinforce-

ing fibers appear bright blue, suggesting that they are composed of stiffened sclerenchyma with thicker, lignified cell walls. These sclerenchyma fibers are embedded in a matrix of irregularly shaped and sized cells that are generally larger than the sclerenchyma cells and appear purplish when dyed. This suggests that these cells are likely the parenchyma “filler” cells, which make up much of the soft, unspecialized tissue found in the plants and whose walls are primarily cellulose [33,35]. These essentially act like a foam matrix with the lignified fibers embedded within. The cells in the thorn are small relative to other parenchyma cells such as those found in potatoes [36], but vary along the longitudinal axis of the thorn. Near the base of the thorn, the major and minor axes of cells were measured to be 121.0 μm (s.d. = 25.9 μm , N = 25) and 44.4 μm (s.d. = 13.7 μm , N = 25), respectively, with cell walls approximately 2.0 μm (s.d. = 0.5 μm). Meanwhile, a closer look at the apex of the thorns reveals that the cells are smaller and more circular with major and minor axes reduced to just 14.8 μm (s.d. = 4.9 μm) and 10.0 μm (s.d. = 4.0 μm , N = 25) with thicker walls approximately 3.7 μm (s.d. = 1.0 μm) across. Approximating the cells as ellipsoids, the volume percentage of the cell walls of the lower thorn was calculated to be just 10%, while in the upper thorn the thicker walls and smaller cells increased this value to 58%. For cellular solids, the effective elastic modulus can be approximated [37] as:

$$\frac{E_{eff}}{E_s} = C_2 \left(\frac{\rho}{\rho_s} \right)^2 \quad (1)$$

where E_{eff} is the effective modulus of the material, E_s is the modulus of the cell walls, C_2 is a constant which can be approximated as 1, ρ is material density, and ρ_s is the density of the cell walls. Using this relationship, the ratio of the effective modulus of the cellular solid at the top of the jackfruit thorn, E_T , to that of the base, E_B can be expressed as:

$$\frac{E_T}{E_B} = \left(\frac{\rho_T}{\rho_B} \right)^2 \quad (2)$$

In the case of the jackfruit thorn the tip can be approximated to be 33.5 times stiffer than the base of the thorn. In fact, this approximation may even be an underestimation since the reinforcing fibers take up proportionally more volume as they near the tip of the thorn and the more elliptical-shaped cells near the base may collapse more easily. This change in cell size and shape can be seen in Fig. S1. This structure gives the jackfruit thorn a gradient in stiffness, a design motif that shows up repeatedly in impact resistant biological materials and has been shown to have beneficial properties like improved fracture toughness and energy dissipation [38].

The lignified fiber bundles continue into the mesocarp but become much thinner; whereas these bundles are 5-6 cells wide in the jackfruit’s exocarp, they transition to only 2-3 cells wide in the mesocarp. Still, the significant amount of blue coloration suggests sporadic lignification throughout the mesocarp layer. The mesocarp layer also exhibits some pink coloration, which is associated with pectin. Recent research suggests that pectin interacts closely with the cellulose in cell walls, forming an interpenetrating network that enhances cross-linking between the cellulose microfibrils [39,40]. Pectin also plays an important role in enhancing cell-to-cell adhesion [40]. In the tubule layer, long pink fibers, one cell in width, run parallel to single-cell blue fibers. Both are embedded in a matrix of cells that are very lightly stained. Finally, the core is mostly pinkish-purple, suggesting less lignification. Furthermore, the core has a sponge-like configuration with the cells acting as struts to form hexagonal pores. These features are illustrated in Fig. 3B.

To further elucidate the composition of each layer, thermogravimetric analysis (TGA) was performed. Fig. 3C shows the pyrolysis curve (normalized sample weight vs. temperature) for each of the

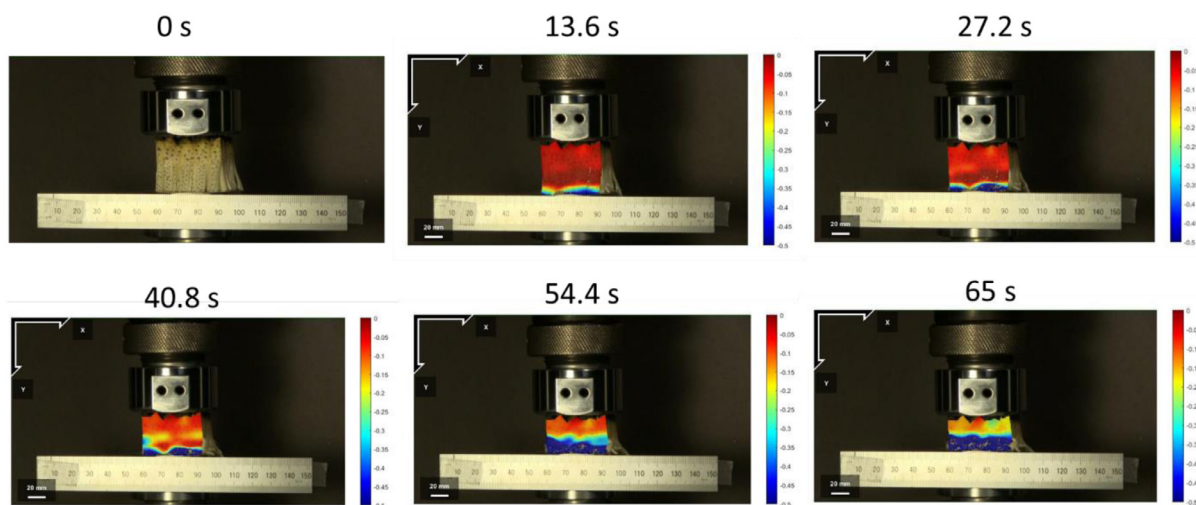


Fig. 4. Digital image correlation of three-layered jackfruit samples compressed at a strain-rate of 10^{-1}s^{-1} . Nearly all of the strain is concentrated in the tubule layer until it has fully collapsed. Color bars indicate the equivalent von Mises strain values where the darkest blue indicates -0.5 and the darkest red is 0.

four layers of the jackfruit while Fig. 3D shows the normalized derivative thermogravimetric (DTG) curve. Fig. 3E plots the amount of residual char vs volatiles in each of the samples. Three of the four layers had nearly the same amount of residual char, about 37%, while the mesocarp samples had about 19% char. This indicates that the mesocarp layer is composed of more volatiles such as hemicellulose, cellulose, and lignin than the other layers which contain more fixed carbon. The normalized DTG curve (Fig. 3D) can be used to obtain further insights into the differences in the composition of the fruit's layers.

An approximate composition of each layer can be inferred from the change in weight of the sample's volatiles in the temperature range for each DTG peak (Fig. 3F) (Table 1). This is discussed in-depth in the supplemental section. As many plant systems contain relatively sparse amounts of pectin, researchers utilizing TG often only include hemicellulose, cellulose, and lignin in their analysis. Since the temperature at which pectin degrades overlaps significantly with the range at which hemicellulose pyrolyzes, the two were combined here. The mesocarp sees a steep drop in mass starting at around 643 K. By this point nearly all of the hemicellulose, pectin, and cellulose should have degraded [41–44], suggesting that the mesocarp is more lignified than the other layers. In many plant systems, lignin acts as reinforcement for the softer tissue surrounding it, conferring rigidity and strength to the cells it fortifies [5,45–47]. Meanwhile, the core displayed elevated levels of pectin, which is often deposited at intercellular joints to enhance cell adhesion [48]. Given the sponge-like structure of the jackfruit's core, containing struts that are single cells wide, cellular adhesion is integral to the performance of this energy-dissipative layer, while the stiffness that would be imbued by lignin is not as important. Likewise, the thorns had the lowest lignin concentration and the largest cellulose concentration, suggesting that the protrusions are meant to function as soft impact dissipators.

The exact mechanical properties of pectin remain mysterious [49] but it has long been known to play a multifunctional role

in plant growth and mechanics [50,51]. When modeling the mechanical behavior of plant fibers, Keryvin et al. [52] assumed the properties of pectin to be the same as those of lignin with promising results, which suggests that the pectin-rich core and lignin-rich mesocarp may have similar mechanical properties. Both the staining and TGA indicate that the tubules contain an intermediate amount of each constituent. However, this highly porous mesostructured layer inherently decreases its effective modulus. This arrangement of a soft ductile material sandwiched between two denser and stiffer layers is a common design motif that is utilized by both nature and engineers to improve impact resistance [38].

3.2. Compressive mechanical behavior

The jackfruit contains a series of sequential failure mechanisms that absorb strain energy and protect its precious seeds. The first layer to fail is the extremely porous, aligned tubular region on the fruit's interior. DIC quasi-static compression tests performed on three-layered samples (thorns, mesocarp, and tubular region) show this phenomenon (Fig. 4). Only after the tubules have almost entirely collapsed do the other two layers begin to deform and absorb strain energy. During an *in-vivo* impact, the initial load should be equally distributed amongst the exterior thorny layer; however, having an easily collapsible porous layer beneath allows for easy transfer of impact energy to the deeper regions of the fruit.

After the tubular layer, the next layer to deform during compression is the thorny exterior. When samples of just mesocarp and thorns were compressed, the thorny layer collapsed first as shown in Fig. 5A. Upon being released, the thorns recovered nearly half of their initial height as can be seen in the last two frames. The underlying structure of the jackfruit thorn also plays a vital role in its compressive and viscoelastic behavior. The surface of the thorns is composed of skin with a highly ordered, microscale wave-like configuration as shown in Fig. 5B. Beneath this wrinkly

Table 1

Temperature for each peak of each layer of the jackfruit. In parentheses is the height of the normalized DTG peak, i.e., the height of the peak relative to that of the layer's highest peak.

	Thorn	Mesocarp	Tubule	Core
Peak 1	487 K (40.3%)	472 K (73.9%)	473 K (58.6%)	478 K (56.8%) [shoulder]
Peak 2	535 K (43.3%) [shoulder]	541 K (86.4%) [shoulder]	532 K (58.6%) [shoulder]	516 K (99.3%)
Peak 3	591 K (100%)	569 K (100%)	584 K (100%)	552 K (100%)
Peak 4	863 K (5.4%)	708 K (36.3%)	898 K (16.4%)	893 K (20%)

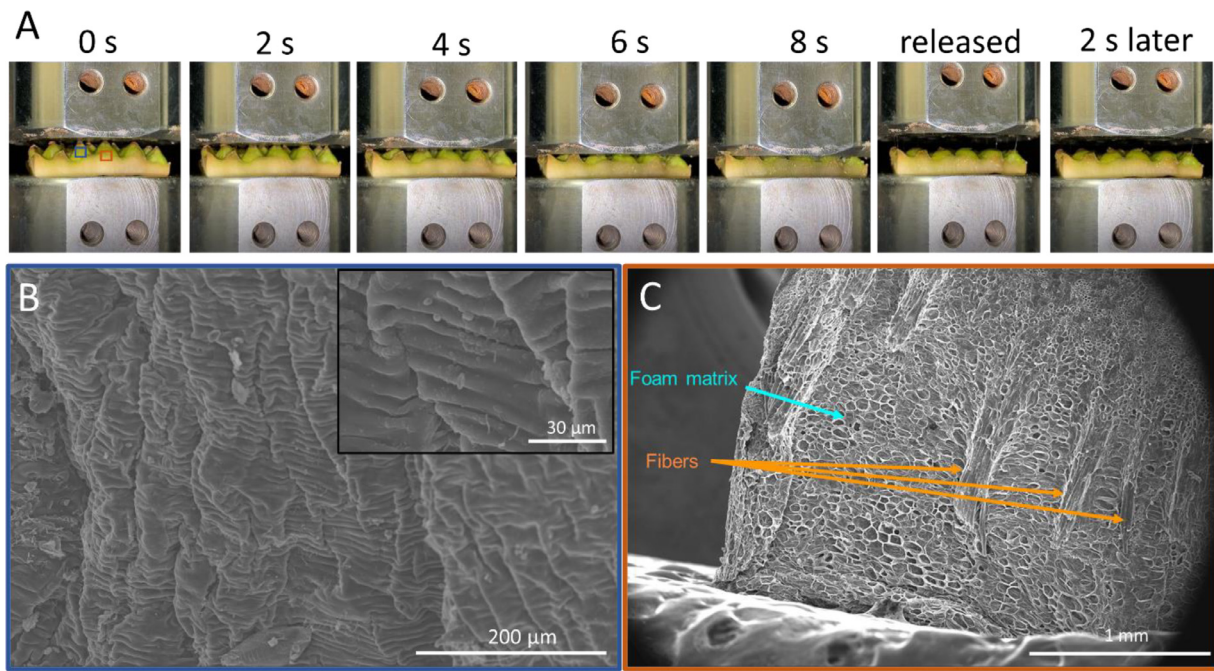


Fig. 5. A.) Images of two-layer jackfruit samples composed of the thorn and mesocarp layer being compressed and released. B.) SEM scans of the jackfruit thorn's ordered exterior and C.) the underlying structure of the jackfruit thorn where the fibers, cellular matrix, and gradient in cell size can be seen. The general location of images B and C are indicated by the boxes on the first panel of A.

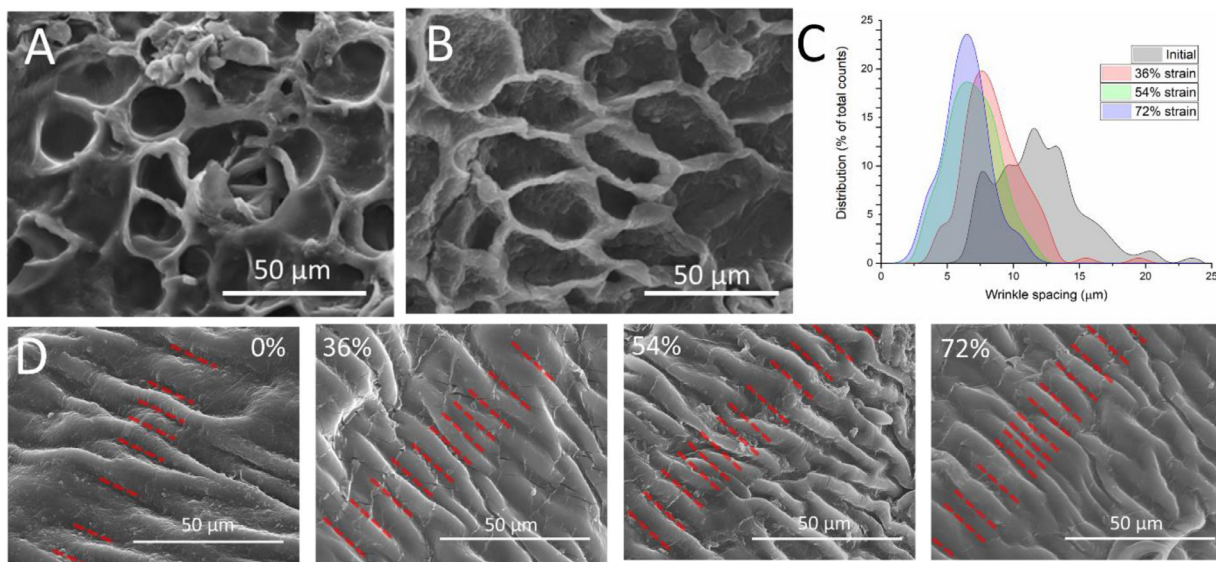


Fig. 6. The thorn structure shows impressive ordered collapse and survivability during compression. A.) A pre-compression image taken of the underlying structure of the jackfruit thorn and B.) an image of the same structure after being compressed to 72%. C.) Distribution of the jackfruit thorn's wrinkle spacing at different compressive strains and D.) representative images visualizing how the wrinkles pack together during compression.

exterior is a fiber-reinforced closed-cell foam-matrix composite, depicted in Fig. 5C.

Thorn samples were compressed and then imaged by SEM, revealing the collapsibility of their microstructure. Figs. 6A and B show images of the underlying foam matrix before compression and at 72% strain, respectively. Buckling of the cell walls can be observed, but very little fracturing can be seen due to the extreme collapsibility of the sample. On the surface, the wrinkled skin behaves like an extended spring. As the thorn is compressed, the distance between wrinkles decreases and the distribution of wrinkle spacing narrows, as shown in Fig. 6C. Fig. 6D shows how these wrinkles bunch together as the strain is increased. The highly or-

dered nature of the surface skin allows the jackfruit thorn to recruit substantial amounts of material to resist compression. Research into thin-walled, crashworthy structures has shown that a progressive, stable collapse mode is often preferable for increased energy absorption during compression [53,54]. The wavy features of the thorn's exterior dictate this collapse mode by providing asymmetric planes of weakness along the length of the thorn that can fold and condense without failing. Furthermore, with minimal plastic deformation during compression, this structure is able to rebound after being compressed, even to high strains.

Figs. 7A-C show a comparison of the stress-strain curves for the different layers at the compressive strain-rates of 10^0 s^{-1} , 10^{-1} s^{-1} ,

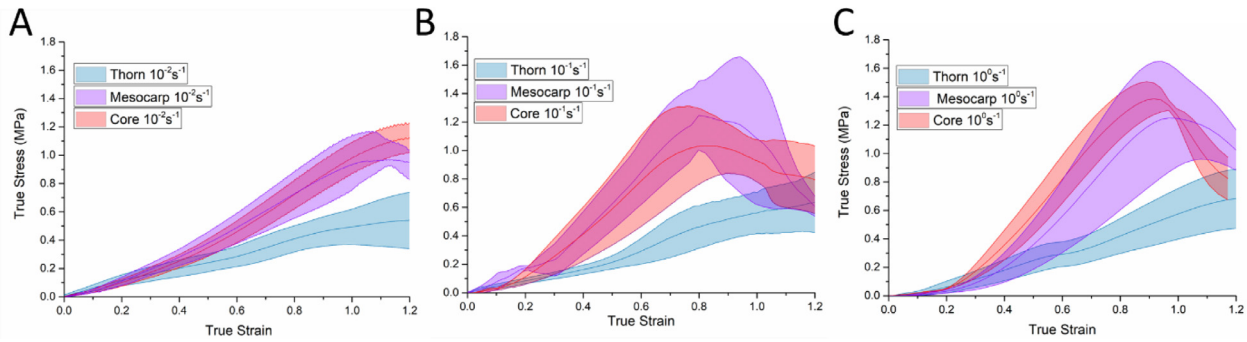


Fig. 7. Comparison of compression true stress-strain response(except the tubule layer) of three layers (except the tubule layer) at three different strain-rates (A. 10^{-2} s^{-1} , B. 10^{-1} s^{-1} , C. and 10^0 s^{-1}).

Table 2

Elastic moduli of each layer at each strain rate.

Strain rate, s^{-1}	Mesocarp, MPa	Core, MPa	Thorn MPa*
10^{-2}	1.19	1.37	3.28
10^{-1}	2.36	1.96	5.15
10^0	2.3	2.38	4.36

* Thorn modulus values are determined using the adjusted cross-sectional area value calculations discussed in Section 3.3.

and 10^{-2} s^{-1} . The elastic moduli of each layer at each strain rate are shown in Table 2.

Across all strain-rates, the behavior of core and mesocarp samples is the most similar, with the core exhibiting a comparable or slightly larger stiffness while the mesocarp was able to reach a higher ultimate stress. Both layers see an increase in stress up until approximately 0.9 strain after which it begins to decrease. The drop in the stress is attributed to fracture and is, as expected, more prominent at high strain rates. As the strain rate is increased, this drop occurs at lower strains.

Thorn samples exhibited the lowest curves, collapsing much more easily at each strain-rate. There is also a noticeable absence of stress drop. This is due partially to the composition of the thorn, but also is a result of the irregular shape of the thorn which leads to a top-down collapse mechanism. With the smallest cross-sectional area, the top of the thorn collapses easily at low loads; however, as the cross-section increases larger and larger loads are required to continue the collapse. The stress calculations for these curves were based on the base cross-sectional dimensions and the result is a steadily rising stress-strain curve. These values do not provide an accurate interpretation of the stress throughout the thorn (which varies due to the changing cross-sectional area). However, it does show the ingenuity of the thorn shape design. The low cross-sectional area at the apex of the thorn allows it to deform at lower loads, absorbing strain energy before other parts of the fruit. There is a parallel with automotive frames that undergo gradual and progressive collapse during impact, protecting the passengers.

The graceful collapse of the thorn discussed previously allows it to compress to very high strains without seeing a drop in load indicative of catastrophic failure (a phenomenon observed for the mesocarp and core samples). The high cellulose content and softer parenchyma cells likely also contribute to the lower stiffness of the thorns. Acting jointly, the macroscale shape, microscale features, and cellular composition enable the thorn to be one of the first parts of the fruit to absorb strain energy during compression while also being capable of doing so to high strains. Furthermore, the thorns exhibit less strain-rate dependence, while the core and mesocarp samples become noticeably stiffer and stronger at higher strain-rates. This ensures that the thorns remain collapsible cush-

ions protecting the body of the fruit during impact. On the other hand, the mesocarp and core layers transition from a steady sloping curve at a strain-rate of 10^{-2} s^{-1} to a stiffer behavior that reaches a maximum stress at ~ 0.8 and ~ 0.95 strain when tested at strain-rates of 10^{-1} s^{-1} and 10^0 s^{-1} , respectively. Interestingly, a trend was observed where samples were able to reach a higher ultimate strain and maximum stress at higher strain-rates. This suggests more energy can be absorbed by these layers during impact scenarios. The drop in stress is associated with failure, which is absent in the thorn layer because of its geometry.

3.3. Viscoelastic behavior

Understanding the viscoelastic nature of the three layers (thorn, mesocarp, and core) can provide insight into their time-dependent behavior. Fig. 8A shows the stress relaxation of the different layers in the jackfruit. Much like with the compressive results, the mesocarp and core have very similar behavior, relaxing to a plateau of about 20% of their initial stress. The thorns relax slightly less; however, this again might be skewed by their irregular shape. Fig. 8B-D shows the relaxation modulus of each layer and their respective fitted curves from the Prony series. The equations describing the resultant Maxwell-Weichert model are listed below:

$$E_{r, \text{core}}(t) = 0.13 + 0.248e^{-t/3.16} + 0.127e^{-t/56.54} \quad (3)$$

$$E_{r, \text{mesocarp}}(t) = 0.273 + 0.652e^{-t/1.63} + 0.562e^{-t/17.39} + 0.173e^{-t/269.53} \quad (4)$$

$$E_{r, \text{thorn}}(t) = 0.14 + 0.131e^{-t/27.76} + 0.094e^{-t/465.81} \quad (5)$$

Keryvin et al. [52] performed nanoindentation stress-relaxation experiments on flax cell walls and identified four characteristic relaxation times of 0.3 s – 0.54 s, 1.4 s – 2.3 s, 7.6 s – 10 s, and 46 s – 54 s. These were attributed to hemicellulose, pectin, amorphous cellulose, and crystalline cellulose, respectively. For macroscale tensile relaxation tests performed on flax fibers, these relaxation times smear together into two characteristic relaxation constants, one of $2.6 \pm 2.4 \text{ s}$ attributed to hemicellulose and pectin and one of $55 \text{ s} \pm 29 \text{ s}$ attributed to cellulose. This aligns well with our results, particularly for the core, which has calculated relaxation times of 3.2 s and 56.5 s. While a three-component model was fitted to each layer, the third component of the core and thorn made an insignificant contribution to the fit and was disregarded. The mesocarp, which contains less cellulose and more lignin as determined by TGA, has a third component with a longer relaxation time. This could be the result of the higher lignin concentration found in the mesocarp. The first and second relaxation times (Fig. 8C) are also lower, which suggests there could be more hemicellulose and less crystalline cellulose in this layer of the jackfruit. The thorns, with

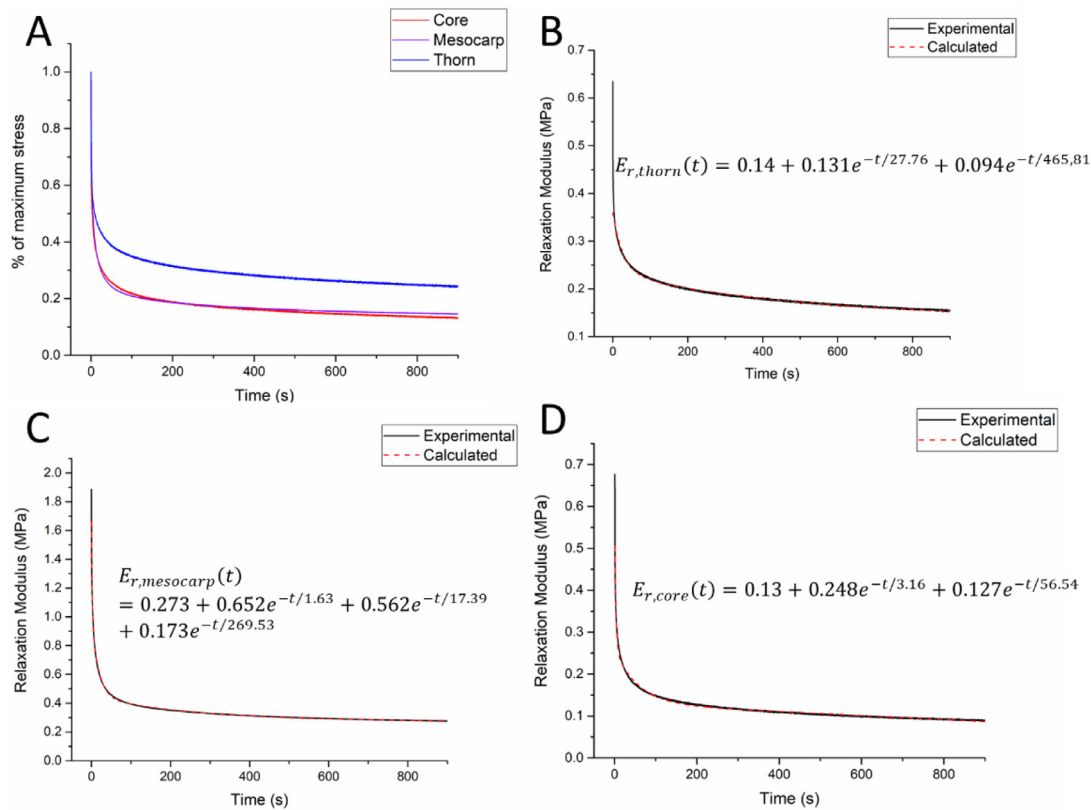


Fig. 8. Stress-relaxation to evaluate the viscoelastic behavior of each layer of the jackfruit (except for the tubular layer). A.) Normalized stress decay curves comparing the core, mesocarp, and thorn layer. B-D.) The experimental relaxation modulus and fitted model for the thorn, mesocarp and core samples during the relaxation test.

the least hemicellulose and pectin, were not determined to have a relaxation constant on the scale of $\tau = 0.1 \text{ s} - 10 \text{ s}$ (Fig. 8B), instead only having an intermediate relaxation constant of 27.8 s and a long-term relaxation constant of 465.8 s. The former is dominated by the cellulose relaxation that is pulled downward by the presence of relatively smaller quantities of more rapidly relaxing hemicellulose and pectin. The larger relaxation time, again, can likely be attributed to the bundles of lignin fibers identified in previous sections.

3.4. Dynamic mechanical behavior

While these quasi-static tests provide insight into the mechanical behavior of the jackfruit, the response of the entire fruit during impact might be quite different. For example, during quasi-static tests on a flat sample, the tubular layer is able to densify entirely, before the mesocarp and thorny layer begin to deform. However, when attached to the entire fruit, this would likely not be possible without tearing the external two layers. Furthermore, under impact conditions the time dependency of stress-waves traveling through the outer two layers may reduce the percentage of strain energy absorbed by the tubular under-layer. To assess this, impact tests using a gas gun were conducted on different combinations of layers.

Fig. 9 shows still images extracted from high-speed footage of the impact event. Samples of mesocarp, mesocarp with thorns, and mesocarp with tubules failed completely. In these cases, the projectile penetrated entirely through the sample, hitting the metal backplate underneath. The mesocarp is composed of aligned fibers that easily peel apart under impact. This can be seen in the tests on the solitary mesocarp samples as well as the tests on the mesocarp and tubule layers, where the tubules begin to absorb the im-

act (row 3, frame 2) but then split apart and fail (row 3, frame 3) before the impactor can be rebounded. For the three-layer samples, nearly all the impact energy was absorbed by the tubule layer which collapsed to strains of ~ 0.3 before rebounding (the rebound could not be captured by DIC as the sample ‘jumped’ off the backplate in the process). This can be seen in DIC figures for the three-layer samples which show minimal strain values in the thorn or mesocarp layers throughout the impact, while the tubule layers collapse. Meanwhile, the thorny layer held the three-layer sample together preventing the splitting observed in the samples of just mesocarp and tubules. When post-impacted samples were cut open, bruising was observed just beneath the thorns for three-layer samples, while samples without thorns were bruised through the whole thickness of the sample.

3.5. Analysis of thorn collapse mechanism

The results indicate that the thorny structure on the surface of the fruit both delocalizes damage while also containing it. When the thorny layer alone was impacted at a lower energy, ultimate failure did not occur. Only the thorns in contact with the projectile exhibited damage. However, each of the impacted thorns experienced a similar level of deformation. Ha et al. [27] observed a similar energy absorption mechanism resulting from the thorny structure of durian fruit. They noted that most of the energy absorbed by the fruit’s exterior could be attributed to bending of the thorns, fracturing at the thorns’ tips, and buckling, bending, and delamination of the thorn’s reinforcing fibers. In the jackfruit, the thorns have a lower aspect ratio, are more densely packed, and are less curved than for durian. Further, the jackfruit’s surface is much more irregular and tends to have less curvature. As a result, the loading mode of the thorns is much closer to axial, leading to a

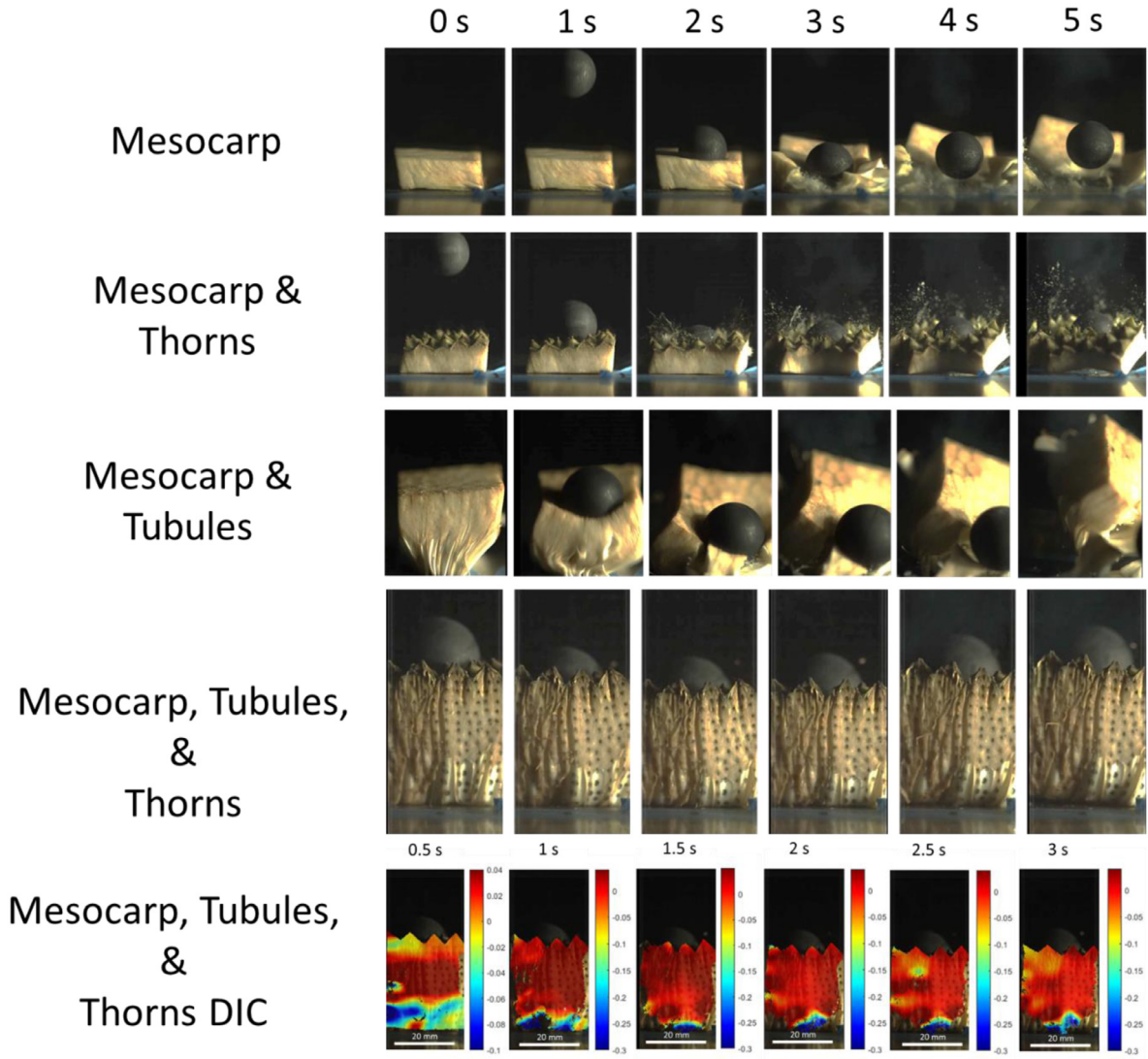


Fig. 9. Still frames extracted from high speed video of gas gun impact tests on different combinations of jackfruit layers. The bottom panels show DIC on three-layer samples during impact. Color bars represent equivalent von Mises strain. The darkest red indicates a strain of 0. In the first frame the maximum strain (dark blue) is -0.1 to show where the strain begins to develop 0.5 seconds after impact. In the subsequent frames the maximum strain is -0.3.

failure mechanism that is dominated by crumpling and, later, splitting of the thorns. The gradient in thorn cell morphology, identified in Section 3, encourages crumpling and buckling near the center of the thorn where the cross-section is still small but where fiber and matrix cell wall density are lower than at the thorn tip.

The shape of the thorn provides an ingenious design for absorbing impact energy, by creating a weak initial contact surface that gradually becomes more resistant to loading as it is compressed. Simplifying the shape of a thorn to be a conical frustrum (Fig. 10A) we can approximate the radius of the thorn at any given height to be

$$r(y) = r_0 + \frac{y}{\tan(\Theta)} \quad (6)$$

where y is the distance to the origin and Θ is the inclination angle of the cone. This can be used to calculate the increase in cross-sectional area as a function of position:

$$A(y) = \pi * \left(r_0 + \frac{y}{\tan(\Theta)} \right)^2 \quad (7)$$

During the elastic portion of thorn compression, the maximum stress occurs at the smallest cross-sectional area, which is the apex

of the pyramid (in our approximation, a cone, if $r_0 = 0$). As such, during elastic compression, the maximum stress is

$$\sigma_{max} = \frac{F}{A(y)} \quad (10)$$

Substituting this in we get

$$\sigma_{max} = \frac{F}{\pi * \left(r_0 + \frac{y}{\tan(\Theta)} \right)^2} \quad (11)$$

Applying this equation to the compression data shown in Fig. 7 results in a near linear increase in stress before a long plateau in stress as the thorn collapses. These results highlight the importance of the shape of the thorn in absorbing energy and cushioning impacts. Furthermore, the distribution in thorn heights leads to an even more gradual macroscopic collapse as certain thorns undergo compression during and axial impact before others.

During compaction, Poisson effects increase the lateral area as the sample is compressed. This can be incorporated into the analysis by assuming that the thorns are incompressible, do not work harden, and are ideally plastic. To simplify the calculations,

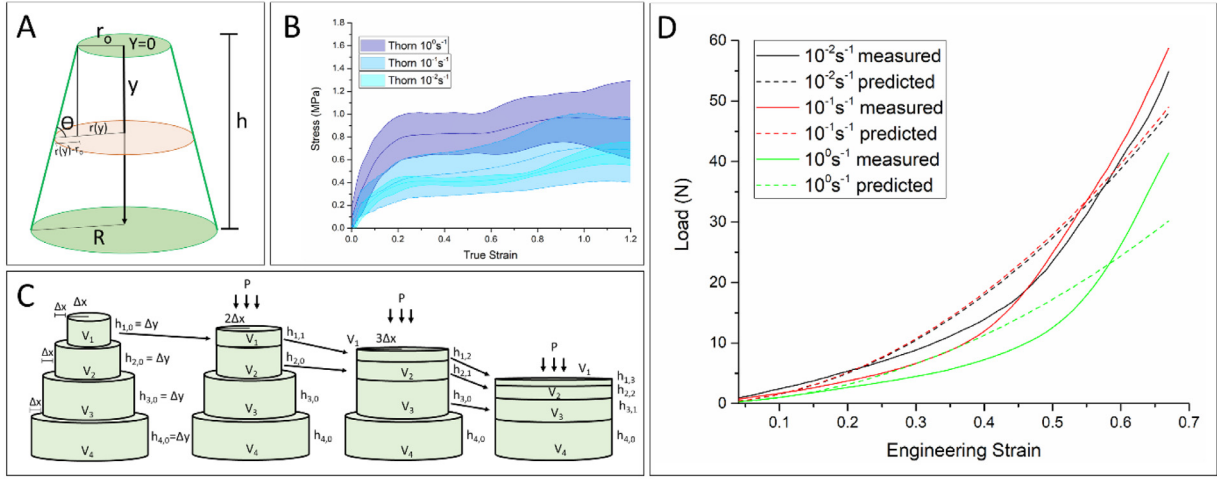


Fig. 10. The shape of the thorn plays a vital role in its compressive behavior. A.) The thorn's shape can be idealized as a conical frustum with a circular cross-section whose radius varies linearly with its height. B.) By accounting for the varied cross-section along the y -axis during compression, the stress in the thorn plateaus after reaching approximately a strain equal to 0.2. C.) The thorn's shape is discretized into stacked cylinders that collapse one at a time until they have a radius equal to the next layer. D.) Average measured load vs. strain curves are plotted alongside estimates using the "wedding cake" model shown in C.

the conical frustum can be discretized into tranches, idealized as stacked cylinders with linearly varying diameters, whose volumes remain constant throughout loading. The force necessary to compress the resulting "wedding cake" model can be ascertained by assuming only the region with the smallest area is being deformed at a given instance. The initial height of each tranche is constant as is the change in radius with each consecutive volume which is determined by the inclination angle, θ , of the thorn. As the top tier is compressed the cross-sectional area increases until it reaches a "merging point", when the area matches that of the next layer. After this step, both are deformed. To denote the height of each layer the notation $h_{n,i}$ was used where n is the layer number beginning with 1 at the top and i is the number of 'times' it has been compressed (i.e., how many other tranches' initial areas it has matched). This notation and collapse process are shown in Fig. 10C. Using the conservation of volume, the height of each layer can be determined using the following equation:

$$h_{n,i} = \frac{n^2}{(n+i)^2} \Delta y \quad (12)$$

Likewise, the strain required to deform the top volume in order to reach the next tranche's area can be calculated using:

$$\epsilon_i = \frac{1+2i}{(1+i)^2} \quad (13)$$

The derivation of these formulas along with other useful equations are provided in the supplementary material. To estimate a force vs. global strain plot for an arbitrarily shaped thorn the following equation is introduced:

$$F = \sigma_F * a(y) \quad (14)$$

where

$$a(y) = \frac{V_{n,i}}{h_{n,i}} \quad (15)$$

and σ_F is a constant flow stress that is estimated using an evolutionary optimization algorithm to reduce the residual sum squares relative to the measured force on the jackfruit thorns. This uses the conservation of volume assumption to account for the lateral expansion of the thorn as it is compressed. Fig. 10D shows both the average measured and predicted load vs strain curves for each strain rate. More accurate models would need to account for the imperfect plasticity of the cell walls and the collapsibility of the

cellular structure of the thorns. These likely lead to the longer load plateau in the empirical curves.

3.6. Fracture propagation paths

Impact reveals a preferential cracking mechanism. Cracks nearly always propagate between the irregular bases of the thorns. Thus, fracture is prevented from spreading throughout the fruit's surface, the irregular hexagonal base configuration leading to tortuous crack paths. The image on the left of Fig. 11A shows the underside of the sample where both the damage control mechanism and the preferential cracking (highlighted by dashed red lines) can be observed. A close look at the cracks also shows that the material has not entirely failed as intact fibers bridge the cracks faces. On the right of Fig. 11A the exterior of the sample after impact can be seen, where splitting, crumpling, and discoloration of just the impacted thorns can be seen. Fig. 11B shows the surface of a splitting jackfruit with significant fiber bridging spanning the valleys between the thorns.

To explore the preferential cracking mechanism in the jackfruit's thorny layer, compact tension specimens were prepared. A pre-crack was introduced and driven through the sample. Much like the cracks that developed during impact testing with a spherical projectile, there was a preferential crack path between the thorns, which is visualized by the still frames shown in Fig. 11C. The extrinsic toughening mechanism of fiber bridging, where fibers span the crack interfaces behind the crack tip, was observed and can be seen in the insets of Fig. 11C. DIC analysis of the compact tension tests can be found in supplemental Fig. S2. The average load vs extension plots for the compact tension tests performed at different crosshead speeds (Fig. 12A) show a clear strain-rate dependency, with the curves of faster crosshead speeds achieving higher loads. As a result, the energy absorbed (the area under the curve), increases with increasing crosshead speed (Fig. 12B).

The sudden rises in load in the load-extension curve correspond to the instant when the crack encounters a thorn. Upon the crack bypassing the thorn, it continues propagating through the valleys between them and the load drops again.

3.7. Collapse stress for tubular layer

It is instructive to determine the contribution of the compressive collapse of the tubules to the energy absorption. The Euler

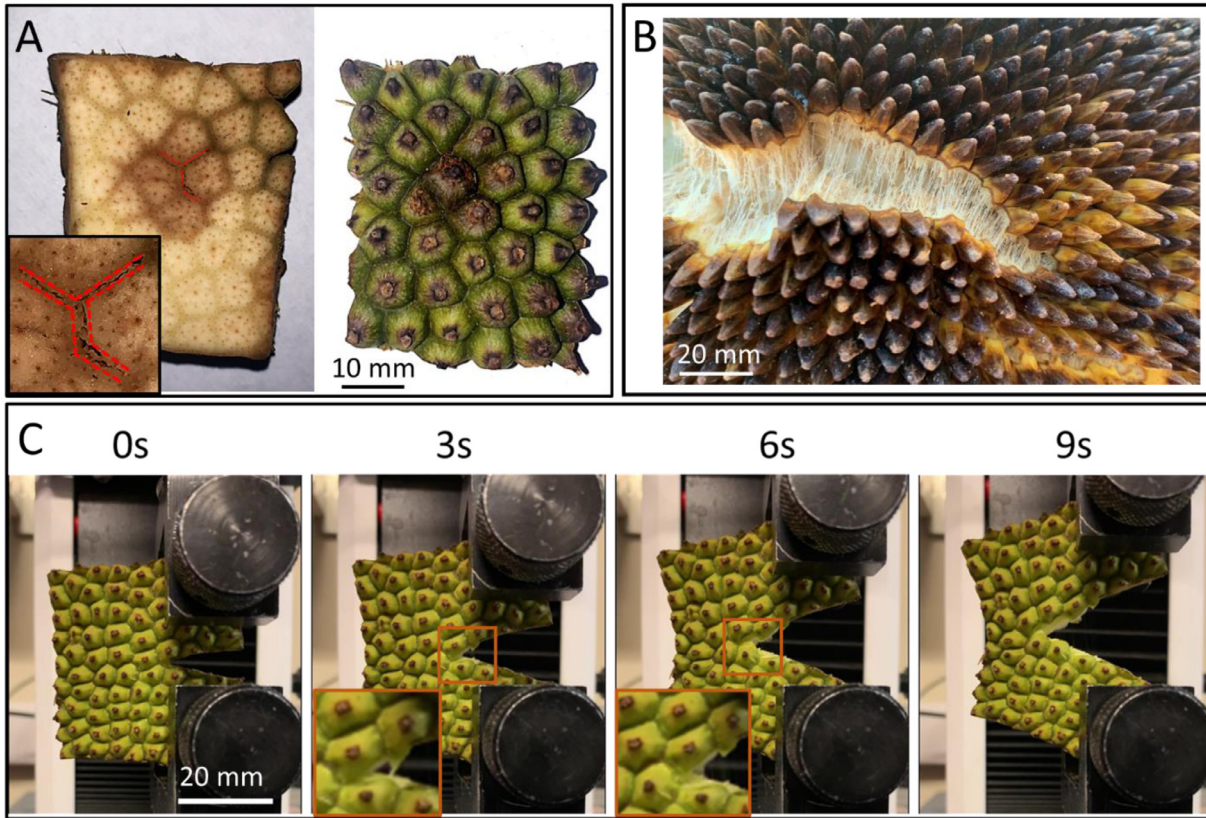


Fig. 11. A.) During projectile impact tests on the thorn jackfruit's thorn structure, cracks propagate preferentially between the thorns. Furthermore, by looking at the underside of thorn samples, bruising can be seen exclusively in the thorns that were in contact with the projectile. B.) Crack propagation along the jackfruit surface between thorns showing significant fiber bridging. C.) Compact tension tests reveal that cracks prefer to propagate between the thorns even when a crack is being driven through the material under slower loading conditions.

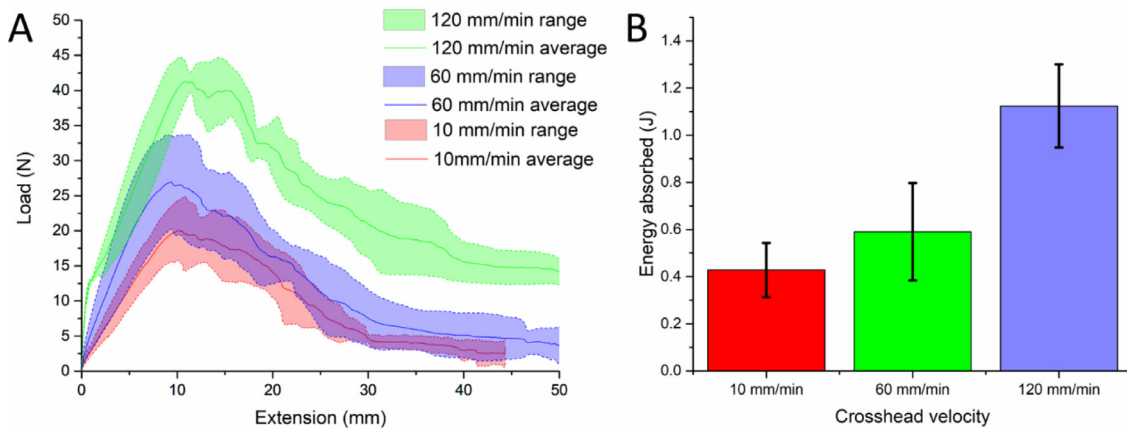


Fig. 12. Compact tension tests at multiple cross-head speeds for the jackfruit's outer later. A.) A clear deformation-velocity dependency can be seen in the load-extension curves. B.) The energy absorbed during compact tension tests increases significantly with an increase in crosshead velocity.

buckling equation provides the simplest approximation. The critical load, P_c , for a tubule is given by:

$$P_c = \frac{\pi EI}{L^2} \quad (12)$$

where E is the Young's modulus and L is the tubule length (assuming pinned joints). The lower moment of inertia I for an elliptical cross-section is:

$$I_x = \frac{\pi}{64} (AB^3 - ab^3) \quad (13)$$

where A and B are the major and minor axes, respectively, of the outer tubule wall and a and b are the major and minor axes, respectively, of the inner wall. The stress is calculated from the number of tubules in a normal cross section per unit area.

The length of the tubule region can vary widely based on the size and age of the fruit; for the purpose of this calculation a prototypical tubule length (5 mm) of one jackfruit specimen was used. Also, owing to the narrow geometry of the tubule walls, it was difficult to calculate the modulus of bulk tubule material directly. Instead, the modulus of the mesocarp, likely the most similar region, was used. Applying the structural parameters measured

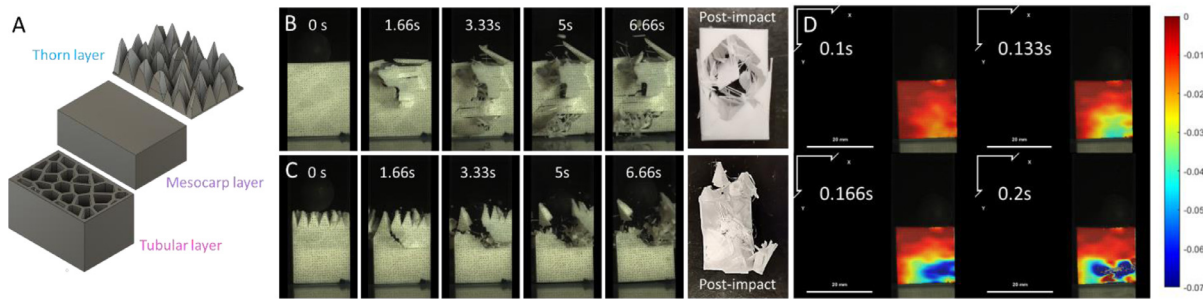


Fig. 13. Bioinspired designs were fabricated to translate the impact resistant mechanism in the jackfruit to engineered materials. A.) An exploded CAD schematic showing the different layers of the bioinspired models. B.) Still images extracted from high-speed video of a featureless control block and C.) a three-layer jackfruit-inspired design during and after impact. D.) DIC analysis of two-layer jackfruit-inspired samples without thorns showing that strain is concentrated in the tubular layer before failure. The maximum equivalent von Mises strain (darkest blue) is -0.07.

in Section 3.1, a critical buckling force of 0.55 N/tubule was calculated using Equation. [13]. With an average area of $3.17 \times 10^{-6} \text{ m}^2$ per tubule and an area fraction of 43.9%, there are approximately 17,000 tubules per square meter. The onset of buckling for each tubule is approximately 0.174 MPa. Assuming the shape of the jackfruit to be an ellipsoid defined by radii, r_x , r_y , and r_z , the surface area of the fruit can be approximated using Knud Thomsen's formula:

$$S = 4\pi \left(\frac{r_x^p r_y^p + r_x^p r_z^p + r_y^p r_z^p}{3} \right)^{\frac{1}{p}} \quad (14)$$

where p is 1.6075. Using the same specimen as before, values of r_x , r_y , and r_z were measured to be, 0.09 m, 0.0105 m, and 0.19 m; the resulting external surface area is 0.2 m^2 (Eq. 15). Subtracting the thickness of the thorn layer (0.005 m) and mesocarp layer (0.01 m) to get the surface area of the underside of the mesocarp, where the tubules terminate, one obtains a surface area of 0.154 m^2 . This implies that there is a total of $\sim 2,600$ tubules in a jackfruit. The simultaneous collapse of the entire tubule layer requires approximately 69.3 N. However, when falling from a tree, impact is not spread evenly over the entire jackfruit but rather primarily across the region below the thorns that impact the surface. Using our previous measurements for the jackfruit sample, the idealized ellipsoid can be described in cartesian coordinates as:

$$\frac{x^2}{0.09^2} + \frac{y^2}{0.0105^2} + \frac{z^2}{0.19^2} = 1 \quad (15)$$

From DIC experiments, it can be seen that the tubules begin to collapse at around $\varepsilon=0.08$ (0.0004 m). The impact area before buckling can be estimated as the intersection of the ellipsoid equation and the plane that is the sum of the thorn height (0.005 m), mesocarp thickness (0.01 m), and compression distance (0.0004 m) beneath the surface of the jackfruit. These planes correspond to $x = 0.0746$, $y = 0.0896$, and $z = 0.1746$. Using the equations by Bektaş [55] we can calculate the area of intersection for each of these planes to be 0.00162 m^2 , 0.00099 m^2 , and 0.00045 m^2 with critical buckling forces of 15.2 N, 9.26 N, and 4.21 N, respectively, depending on which side the jackfruit lands on.

To determine the maximum force exerted on the jackfruit during impact, free fall tests were performed to determine the deflection of the fruit during dynamic loading. A fruit weighing 6.97 kg was dropped from a height of 7.62 m onto a concrete slab. Just before impact the diameter of the fruit was 0.24 m. When the velocity of the fruit drops to zero, the diameter was measured to be 0.2124 m, indicating a change of 0.0276 m. Using this value as the deceleration distance and assuming the concrete slab to be inelastic, conservation of energy can be used to estimate that the maximum dynamic force exerted on the fruit was approximately 18.9 kN, approximately one thousand times the collapse force for the

tubular layer. Hence, the initial buckling of the tubules cannot account for a significant fraction of the energy dissipation.

3.8. Bioinspiration from the jackfruit

In order to demonstrate that the jackfruit structure can be translated to an engineered system, impact tests were performed on 3D printed designs, comprised of combinations of thorns, featureless mesocarp, and tubular layers. Fig. 13A shows an exploded schematic of these layer designs. A variety of print materials were explored to understand which engineering scenarios are best suited for the use of the jackfruit design.

The first series of tests was printed out of relatively stiff, brittle PETG. Blocks of solid PETG were printed at decreasing increments of infill and tested until samples consistently failed. Jackfruit-inspired designs were then scaled to the same size as the control block and printed to be the same mass. For the first test, a control block of PETG printed with 10% infill was used for comparison. Fig. 13B shows the total failure of the control as the projectile travels through the entire length of the sample, causing fractures to initiate and propagate between the print layers in the process. The jackfruit-inspired sample, shown in Fig. 13C, sustained considerably less through-thickness damage. Owing to the fact that PETG is considerably stiffer than natural jackfruit, the impact stress was not effectively transmitted through the sample layers. The result is that the progressive collapse mechanism of tubule buckling, followed by thorn compression, before finally giving way to mesocarp densification, was not observed. DIC analysis showed minimal strain (<0.01) in the tubular and mesocarp layer throughout the impact event. However, despite the mismatch in material properties, the thorn structure still efficiently absorbed impact energy and delocalized damage across the sample surface. This mechanism can be observed in the post-impact still images of the samples, where the neat, control block has a hole approximately the same size as the impactor through its entirety, whereas the lower layers of the jackfruit-inspired sample are still intact while the outer thorn layer is completely obliterated. During impact, the thorns directly beneath the projectile collapse downward along their longitudinal axis, splitting vertically as they do, while adjacent thorns in contact with the impactor buckle and bend before snapping. Nearby thorns that are not in the impact zone provide lateral planes of weakness that encourage damage to spread horizontally through the sample rather than vertically. Samples printed with tubules but without the thorns exhibited strain concentrations in the tubular layer before failing. Fig. 13D shows strain maps of these samples during impact. Due to the high stiffness of PETG minimal buckling, bending, or deformation was observed in the tubule layer with fractures initiating at strain values of about 0.067. However, much like biological jackfruit samples, nearly all

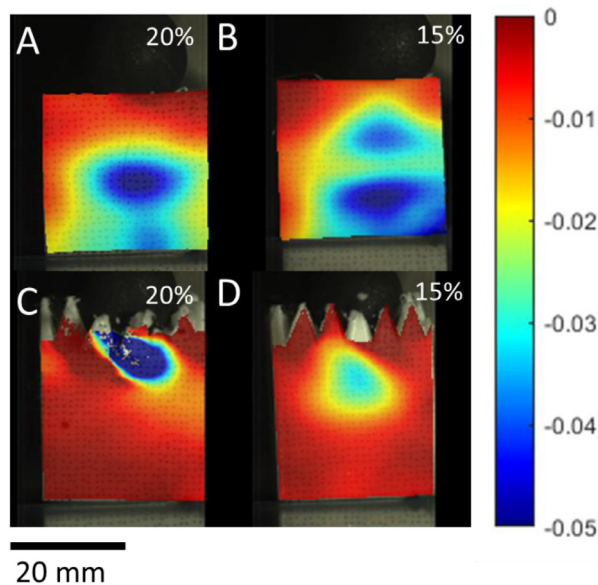


Fig. 14. DIC analysis of A.) tubule and mesocarp samples printed at 20% and B.) 15% infill and three-layer samples printed at C.) 20% and D.) 15% infill just before cracking initiates. In samples without thorns, strain is concentrated in the tubular layer while samples with thorns exhibit the most strain just below the thorns. The maximum equivalent von Mises strain plotted in this figure (darkest blue) is -0.05 .

the strain was concentrated in the tubular layer, as was the resultant damage.

To further understand the interplay between the thorn and tubular layers, samples with higher infills of 15% and 20%, which would fail less easily, were printed. Fig. 14 shows strain maps of impacted samples just prior (<0.033 s) to the onset of fracture. Fig. 14A and B show samples printed without thorns at infills of 20% and 15%, respectively. In these samples, the strain is concentrated in the tubular region, which reaches a maximum of 0.052 at 20% infill and 0.066 for the more flexible 15% infill before failing. Meanwhile, in samples that have thorns, the strain in the tubular region remains below 0.01 for the duration of the impact; most of the strain is spread amongst the thorns and the area just beneath them as shown in Fig. 14C and D. The more flexible 15% infill sample allows the strain to spread deeper and more broadly into the mesocarp layer. These results confirm that the thorns act as an initial barrier to impact and disperse the strain energy near the surface much more effectively than a flat exterior. The latter surface configuration would allow the impact energy to be transmitted deeper into the material. However, the progressive failure of the layers is inverted for the stiffer PETG samples which see failure of the thorns first and then of the tubules, unlike the jackfruit samples. Regardless, both mechanisms continue to exist in stiffer samples.

This energy dispersion mechanism has an effect on how the samples fail during impact. Fig. 15 shows the progression of damage for samples of mesocarp and tubules (A and B), for all three layers (C and D), and tubules and thorns (E and F). In samples, without thorns (A and B) linear cracks form vertically through the sample, causing splitting between the tubules and sample failure. Generally, only a few large cracks were observed which split the sample in half or broke off large chunks of material. In samples with thorns, however, arcing cracks formed just below the thorn layer and moved horizontally through the sample. Many smaller cracks were observed between and through thorns which propelled debris in every direction. While several cracks reached the tubular layer, none were observed traveling all the way through the samples which were still intact after testing. To de-

termine whether this was simply the result of more material in the three-layer samples, designs of just thorns and mesocarp were fabricated which have significantly less material. Still, no cracks traveled entirely through the sample, while crack arcing, multiple cracking, and large amounts of impact debris were still observed. The tubules absorb strain energy by acting as a weak, porous layer that can easily collapse before the solid mesocarp layer. This effect is decreased in stiffer samples yet was still observed in those without thorns. This suggests that the tubule layer would be the next to compress and fracture if impacted with more energy.

3.9. Discussion of main results

The jackfruit is the largest fruit on the Earth and is capable of withstanding very high falling impacts. The goals of this study were (a) to understand how the jackfruit is able to survive such events and (b) to apply these concepts to bioinspired designs.

For this, the structure and composition of the jackfruit's layers was characterized for the first time.

1. MicroCT scans revealed a tubular layer that has a porosity of approximately 57% while SEM scans showed that the thorns on the exterior of the jackfruit have a fiber-reinforced foam composite structure and are covered with an ordered, wavy skin.
2. These fibers are lignified while the surrounding matrix is primarily composed of cellulose-rich parenchyma cells that increase in size and decrease in wall thickness towards the base of the thorn. As a result, the tip has a much higher cell wall density than the base.
3. The thorns have a significantly higher concentration of cellulose while the mesocarp has relatively more lignin and the core contains pectin/hemicellulose. These results corroborate those of the staining experiments and agree well with other studies.

These structural and compositional findings were then connected to the behavior of each of the jackfruit's layers with mechanical tests.

1. The lignin-rich mesocarp and pectin/hemicellulose rich core behave relatively similarly, with the mesocarp samples generally reaching higher ultimate stresses. This suggests that these two layers form a sandwich structure around the tubular layer which collapses first when the outer three layers are compressed together.
2. The thorn on the other hand, even when adjusted for its variable cross-section, plateaued at a relatively low stress value but did not see a decrease even when compressed to 30% of its original height. This is optimal for continuously absorbing impact energy during falling, when the exterior of the fruit can experience very high strains. The conical structure of the jackfruit thorn is also ideal for absorbing impact energy. As the strain on the thorn increases, so does the cross-sectional area. This means that the apex of the thorn absorbs the brunt of the impact energy by collapsing easily, while the increasing cross-sectional area leads to a gradual increase in resistance. Ultimately, this makes the thorn an ideal impact surface energy-absorber.
3. The irregular hexagonal base structure not only allows for optimal packing of the thorns, but it also leads to increased crack tortuosity both during impact testing and during compact tension tests. Cracks prefer to initiate between the thorns and propagate around them rather than traveling through them. Furthermore, the thorn structure delocalizes damage across the surface of the jackfruit.
4. Compact tension tests reveal that even when driven through the jackfruit skin, cracks prefer to travel between the thorns. The skin also absorbs more energy during compact tension tests at faster crosshead speeds.

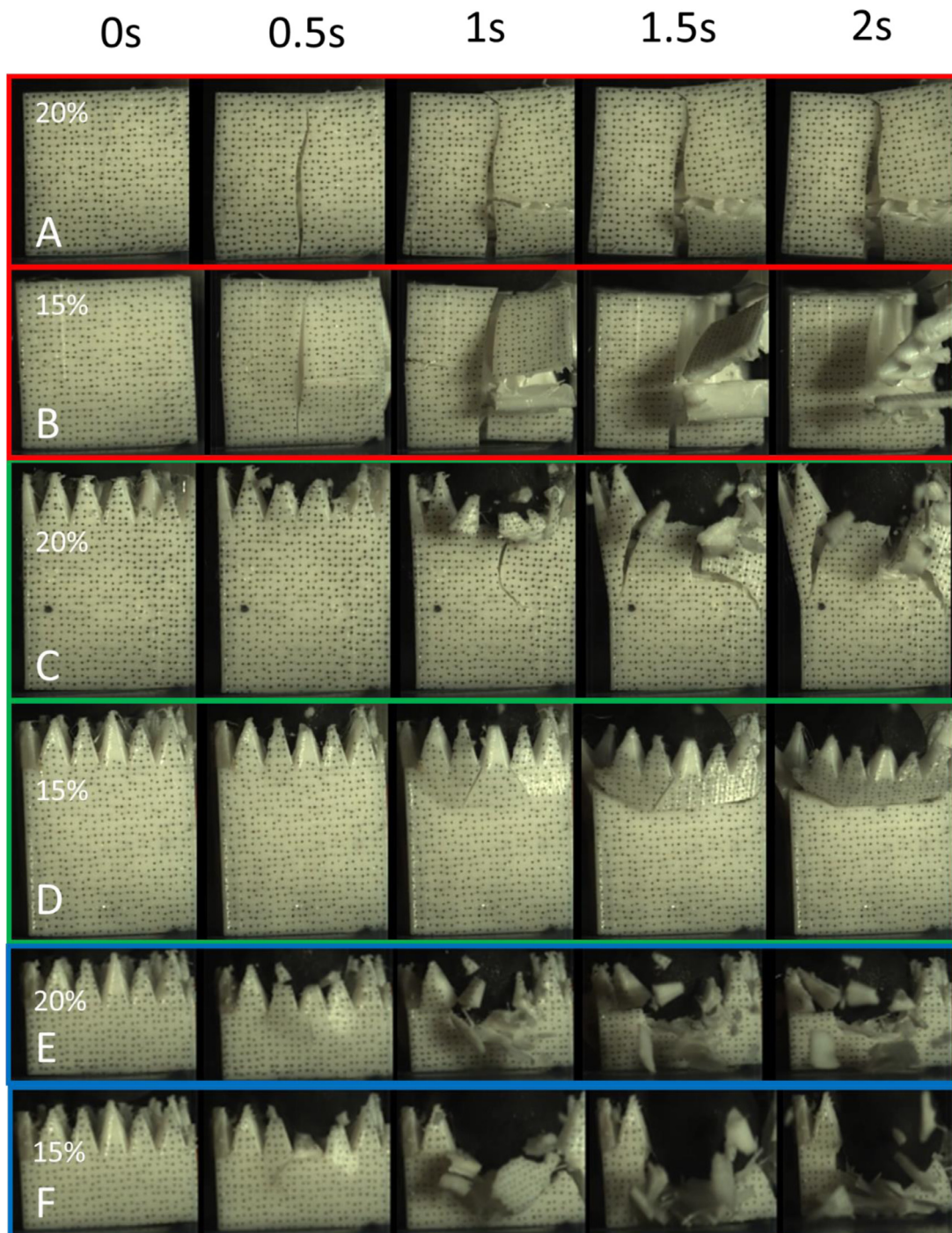


Fig. 15. Extracted still images from high-speed video of gas gun impact tests on tubule and mesocarp samples printed at A.) 20% and B.) 15% infill, three-layer samples printed at C.) 20% and D.) 15% infill, and thorn and mesocarp samples printed at E.) 20% and F.) 15% infill.

The general structure of the jackfruit was then transferred to bioinspired designs to capture its mechanical capabilities.

1. During impact, the thorn structure effectively spreads damage across the surface of the sample at all infills. Meanwhile, control samples of the same mass punctured through their full thickness at low infills or experienced ultimate failure due to vertical cracking at high infills.
2. In three-layer samples, strain was concentrated in the thorn layer during impact, while in two-layer samples composed of just a bioinspired mesocarp and tubular layer, nearly all of the pre-failure strain developed in the deeper tubular layer.

These tests show that jackfruit-inspired designs can be successfully utilized to improve the impact resistance of engineered materials. The thorn structure is a particularly useful design motif for several reasons:

1. It can be transferred to materials with different properties (i.e., stiffness) while still providing benefits: Many bioinspired designs need to be replicated using materials that contain properties akin to those of the natural system. However, the thorn structure disperses impact damage along the surface of a material in both stiff and soft materials.

- It can be easier to fabricate: Unlike other common bioinspired designs that resist impact like conch shells or horse hooves, the thorn structure is not inherently composite and can be fabricated out of a single material, making it easier to manufacture.
- It can be combined with other designs: Many biological systems use composite interfaces as a means of fracture control [56] to improve impact resistance, but these mechanisms break-down, particularly near the surface, during impact scenarios [4]. Yet the thorn structure can yield preferential, tortuous cracking during impacts, even while using just a single material. This a flexible design can easily be combined with other toughening architectures to act as a first contact surface structure that reduces impact damage and channels initial cracking.

4. Conclusions

In the present study, several impact resistant mechanisms in the jackfruit were identified. The exterior thorns have a fiber-reinforced composite structure and an ordered wavy surface which condenses when compressed. The conical shape of the thorns also contributes to the impact resistance of the fruit by containing fractures to interstitial valleys, dispersing damage across the surface, and gradually increasing the cross-sectional area of the impacted surface as the thorn is compressed. A simplified model of thorn collapse is put forward to describe the effect of the conical shape on the axial crushing force of the thorn. The composition and porosity of the jackfruit's different layers also result in a progressive collapse mechanism where deformation in standalone specimens is led by the tubule region before the thorns and ultimately the mesocarp. Gas gun tests confirm that this helps cushion impacts while spreading damage to the fruit along the surface. Jackfruit-inspired, 3D printed samples exhibited less through-thickness damage than controls samples during impact tests and showed that these mechanisms can be transferred to engineered materials.

Declaration of Competing Interest

The authors declare that they have no known competing financial interests or personal relationships that could have appeared to influence the work reported in this paper.

Acknowledgements

We acknowledge funding from the National Science Foundation Mechanics of Materials and Structures program (Grant number 1926361). Discussions with Professor Iwona Jasiuk are gratefully acknowledged. We would like to thank Professor Robert Sah and Dr. Albert Chen for their help with the CT scans as well as Isaac Cabrera for his help with the DIC analysis as well as Isaac Cabrera. We would like to thank Sabine Faulhaber and the Nano-Engineering Materials Research Center as well as Nano3 for their help in obtaining SEM images. Gas gun tests were made possible thanks to Ryan Fanher and Professor Nicholas Boechler's lab. The help provided by Professor Boechler was extremely valuable. Finally, we would like to thank Dr. Pollyana Cardoso and Marcelo Ueki for their help performing the thermal characterization tests and Diego de Carvalho Carneiro for his help with staining and optical microscopy.

Supplementary materials

Supplementary material associated with this article can be found, in the online version, at [doi:10.1016/j.actbio.2023.04.040](https://doi.org/10.1016/j.actbio.2023.04.040).

References

- C.W. Wu, Z.D. Zhu, W. Zhang, How woodpecker avoids brain injury? J. Phys. Conf. Ser. (2015) 628012007, doi:10.1088/1742-6596/628/1/012007.
- S. Dike, W. Yang, A. Pissarenko, H. Quan, F.C. Garcia Filho, R.O. Ritchie, M.A. Meyers, On the gular sac tissue of the brown pelican: structural characterization and mechanical properties, Acta Biomater 118 (2020) 161–181, doi:10.1016/j.actbio.2020.10.008.
- B. Wang, T.N. Sullivan, A. Pissarenko, A. Zaheri, H.D. Espinosa, M.A. Meyers, Lessons from the ocean: whale baleen fracture resistance, Adv. Mater. 31 (2019) 1804574, doi:10.1002/adma.201804574.
- H. Li, J. Shen, Q. Wei, X. Li, Dynamic self-strengthening of a bio-nanostructured armor – conch shell, Mater. Sci. Eng. C. 103 (2019) 109820, doi:10.1016/j.msec.2019.109820.
- A.K. Matsushita, D. Gonzalez, M. Wang, J. Doan, Y. Qiao, J. Mckittrick, Beyond density: mesostructural features of impact resistant wood, Mater. Today Commun. 22 (2020) 100697, doi:10.1016/j.mtcomm.2019.100697.
- R. Seidel, M. Thielen, C. Schmitt, A. Bührig-Polaczek, C. Fleck, T. Speck, Fruit walls and nut shells as an inspiration for the design of bio-inspired impact-resistant hierarchically structured materials, Int. J. Des. Nat. Ecodyn. 8 (2013) 172–179, doi:10.2495/DNE-V8-N2-172-179.
- B. Wang, B. Pan, G. Lubineau, Morphological evolution and internal strain mapping of Pomelo peel using X-ray computed tomography and digital volume correlation, Mater. Des. 137 (2018) 305–315, doi:10.1016/j.matdes.2017.10.038.
- M. Thielen, C.N.Z. Schmitt, S. Eckert, T. Speck, R. Seidel, Structure–function relationship of the foam-like pomelo peel (*Citrus maxima*)—an inspiration for the development of biomimetic damping materials with high energy dissipation, Bioinspir. Biomim. 8 (2013) 25001, doi:10.1088/1748-3182/8/2/025001.
- A. Bührig-Polaczek, C. Fleck, T. Speck, P. Schüler, S.F. Fischer, M. Caliaro, M. Thielen, Biomimetic cellular metals—using hierarchical structuring for energy absorption, Bioinspir. Biomim. 11 (2016) 45002, doi:10.1088/1748-3190/11/4/045002.
- M. Thielen, T. Speck, R. Seidel, Viscoelasticity and compaction behaviour of the foam-like pomelo (*Citrus maxima*) peel, J. Mater. Sci. (2013), doi:10.1007/s10853-013-7137-8.
- W. Zhang, S. Yin, T.X. Yu, J. Xu, Crushing resistance and energy absorption of pomelo peel inspired hierarchical honeycomb, Int. J. Impact Eng. 125 (2019) 163–172, doi:10.1016/j.ijimpeng.2018.11.014.
- T.-T. Li, H. Wang, S.-Y. Huang, C.-W. Lou, J.-H. Lin, Bioinspired foam composites resembling pomelo peel: Structural design and compressive, bursting and cushioning properties, Compos. Part B 172 (2019) 290–298, doi:10.1016/j.compositesb.2019.04.046.
- I. Schäfer, M. Mlikota, S. Schmauder, U. Weber, Modelling the damping response of biomimetic foams based on pomelo fruit, Comput. Mater. Sci. 183 (2020) 109801, doi:10.1016/j.commatsci.2020.109801.
- F. Du, T. Tan, Recent studies in mechanical properties of selected Hard-Shell seeds: a review, JOM 73 (2021) 1723–1735, doi:10.1007/s11837-021-04688-w.
- P. Schüler, T. Speck, A. Bührig-Polaczek, C. Fleck, Structure-function relationships in *Macadamia integrifolia* seed coats – fundamentals of the hierarchical microstructure, PLoS One 9 (2014) 1–14, doi:10.1371/journal.pone.0102913.
- M. Sonogo, C. Fleck, L.A. Pessan, Mesocarp of Brazil nut (*Bertholletia excelsa*) as inspiration for new impact resistant materials, Bioinspir. Biomim. 14 (2019), doi:10.1088/1748-3190/ab2298.
- V.M. Scussel, D. Manfio, G.D. Savi, E.H.S. Moecke, Stereoscopic and scanning electron microscopy of Brazil nut (*Bertholletia excelsa* H.B.K.) shell, brown skin, and edible part: Part One—healthy nut, J. Food Sci. 79 (2014) 1443–1453, doi:10.1111/1750-3841.12502.
- M. Sonogo, C. Fleck, L.A. Pessan, Hierarchical levels of organization of the Brazil nut mesocarp, Sci. Rep. 10 (2020) 6786, doi:10.1038/s41598-020-62245-y.
- B. Gludovatz, F. Walsh, E.A. Zimmermann, S.E. Naleway, R.O. Ritchie, J.J. Kruzic, Multiscale structure and damage tolerance of coconut shells, J. Mech. Behav. Biomed. Mater. 76 (2017) 76–84, doi:10.1016/j.jmbbm.2017.05.024.
- N. Graupner, D. Labonte, H. Humburg, T. Buzkan, A. Dörgens, W. Kelterer, J. Müssig, Functional gradients in the pericarp of the green coconut inspire asymmetric fibre-composites with improved impact strength, and preserved flexural and tensile properties, Bioinspir. Biomim. 12 (2017) 026009, doi:10.1088/1748-3190/aa5262.
- X.T. Nguyen, S. Hou, T. Liu, X. Han, A potential natural energy absorption material – coconut mesocarp: Part A: Experimental investigations on mechanical properties, Int. J. Mech. Sci. 115–116 (2016) 564–573, doi:10.1016/j.ijmecsci.2016.07.017.
- S. Schmier, M. Jentzsch, T. Speck, M. Thielen, Fracture mechanics of the endocarp of *Cocos nucifera*, Mater. Des. 195 (2020) 108944, doi:10.1016/j.matdes.2020.108944.
- E.A. Flores-Johnson, J.G. Carrillo, C. Zhai, R.A. Gamboa, Y. Gan, L. Shen, Microstructure and mechanical properties of hard *Acrocomia mexicana* fruit shell, Sci. Rep. 8 (2018) 9668, doi:10.1038/s41598-018-27282-8.
- S.J. Antreich, J.C. Huss, N. Xiao, A. Singh, N. Gierlinger, The walnut shell network: 3D visualisation of symplastic and apoplasmic transport routes in sclerenchyma tissue, Planta 256 (2022) 49, doi:10.1007/s00425-022-03960-w.
- J. Nicolás-Bermúdez, I. Arzate-Vázquez, J.J. Chanona-Pérez, J.V. Méndez-Méndez, M.J. Perea-Flores, G.A. Rodríguez-Castro, R.N. Domínguez-Fernández, Characterization of the hierarchical architecture and micromechanical properties of walnut shell (*Juglans regia* L.), J. Mech. Behav. Biomed. Mater. 130 (2022) 105190, doi:10.1016/j.jmbbm.2022.105190.

- [26] E. Ahmadi, H. Barikloo, M. Kashfi, Viscoelastic finite element analysis of the dynamic behavior of apple under impact loading with regard to its different layers, *Comput. Electron. Agric.* (2016), doi:[10.1016/j.compag.2015.11.017](https://doi.org/10.1016/j.compag.2015.11.017).
- [27] N.S. Ha, G. Lu, D. Shu, T.X. Yu, Mechanical properties and energy absorption characteristics of tropical fruit durian (*Durio zibethinus*), *J. Mech. Behav. Biomed. Mater.* 104 (2020) 103603, doi:[10.1016/j.jmbbm.2019.103603](https://doi.org/10.1016/j.jmbbm.2019.103603).
- [28] O. Prakash, R. Kumar, A. Mishra, R. Gupta, *Artocarpus heterophyllus* (Jackfruit): an overview, *Pharmacogn. Rev.* 3 (2009) 353.
- [29] C.R. Elevitch, H.I. Manner, *Artocarpus heterophyllus* (jackfruit), *Species Profiles Pacific Isl. Agrofor.* 10 (2006) 1–25.
- [30] J. Schindelin, I. Arganda-Carreras, E. Frise, V. Kaynig, M. Longair, T. Pietzsch, S. Preibisch, C. Rueden, S. Saalfeld, B. Schmid, J.-Y. Tinevez, D.J. White, V. Hartenstein, K. Eliceiri, P. Tomancak, A. Cardona, Fiji: an open-source platform for biological-image analysis, *Nat. Methods.* 9 (2012) 676–682, doi:[10.1038/nmeth.2019](https://doi.org/10.1038/nmeth.2019).
- [31] D. Legland, I. Arganda-Carreras, P. Andrey, MorphoLibJ: integrated library and plugins for mathematical morphology with ImageJ, *Bioinformatics* 32 (2016) 3532–3534, doi:[10.1093/bioinformatics/btw413](https://doi.org/10.1093/bioinformatics/btw413).
- [32] J. Ollion, J. Cochenec, F. Loll, C. Escudé, T. Boudier, TANGO: a generic tool for high-throughput 3D image analysis for studying nuclear organization, *Bioinformatics* 29 (2013) 1840–1841, doi:[10.1093/bioinformatics/btt276](https://doi.org/10.1093/bioinformatics/btt276).
- [33] P. Pradhan Mitra, D. Loqué, Histochemical staining of *Arabidopsis thaliana* secondary cell wall elements, *J. Vis. Exp.* (2014) 51381, doi:[10.3791/51381](https://doi.org/10.3791/51381).
- [34] L. Fukshansky, Revisiting the hexagonal lattice: on optimal lattice circle packing, *Elem. Der Math.* 66 (2011) 1–9.
- [35] T.P. O'Brien, N. Feder, M.E. McCully, Polychromatic staining of plant cell walls by toluidine blue O, *Protoplasma* 59 (1964) 368–373.
- [36] D.G. Hepworth, D.M. Bruce, A method of calculating the mechanical properties of nanoscopic plant cell wall components from tissue properties, *J. Mater. Sci.* 35 (2000) 5861–5865, doi:[10.1023/A:1026716710498](https://doi.org/10.1023/A:1026716710498).
- [37] M.F. Ashby, The mechanical properties of cellular solids, *Metall. Trans. A.* 14 (1983) 1755–1769, doi:[10.1007/BF02645546](https://doi.org/10.1007/BF02645546).
- [38] B.S. Lazarus, A. Velasco-Hogan, T. Gómez-del Río, M.A. Meyers, I. Jasiuk, A review of impact resistant biological and bioinspired materials and structures, *J. Mater. Res. Technol.* 9 (2020) 15705–15738, doi:[10.1016/j.jmrt.2020.10.062](https://doi.org/10.1016/j.jmrt.2020.10.062).
- [39] C.T. Anderson, Pectic polysaccharides in plants: structure, biosynthesis, functions, and applications, in: E. Cohen, H. Merzendorfer (Eds.), *Extracellular Sugar-Based Biopolymers Matrices*, Springer International Publishing, Cham, 2019, pp. 487–514, doi:[10.1007/978-3-030-12919-4_12](https://doi.org/10.1007/978-3-030-12919-4_12).
- [40] D. Wang, T.H. Yeats, S. Uluisik, J.K.C. Rose, G.B. Seymour, Fruit softening: revisiting the role of pectin, *Trends Plant Sci* 23 (2018) 302–310, doi:[10.1016/j.tplants.2018.01.006](https://doi.org/10.1016/j.tplants.2018.01.006).
- [41] M. Amutio, G. Lopez, R. Aguado, M. Artetxe, J. Bilbao, M. Olazar, Kinetic study of lignocellulosic biomass oxidative pyrolysis, *Fuel* 95 (2012) 305–311, doi:[10.1016/j.fuel.2011.10.008](https://doi.org/10.1016/j.fuel.2011.10.008).
- [42] M.A. Lopez-Velazquez, V. Santes, J. Balmaseda, E. Torres-García, Pyrolysis of orange waste: a thermo-kinetic study, *J. Anal. Appl. Pyrolysis.* 99 (2013) 170–177, doi:[10.1016/j.jaap.2012.09.016](https://doi.org/10.1016/j.jaap.2012.09.016).
- [43] J.J.M. Orfão, F.J.A. Antunes, J.L. Figueiredo, Pyrolysis kinetics of lignocellulosic materials—three independent reactions model, *Fuel* 78 (1999) 349–358, doi:[10.1016/S0016-2361\(98\)00156-2](https://doi.org/10.1016/S0016-2361(98)00156-2).
- [44] D. Díez, A. Urueña, R. Piñero, A. Barrio, T. Tamminen, Determination of hemi-cellulose, cellulose, and lignin content in different types of biomasses by thermogravimetric analysis and pseudocomponent kinetic model (TGA-PKM Method), *Process.* 8 (2020). 10.3390/pr8091048.
- [45] M. Rüggeberg, T. Speck, O. Paris, C. Lapiere, B. Pollet, G. Koch, I. Burgert, Stiffness gradients in vascular bundles of the palm *Washingtonia robusta*, *Proc. R. Soc. B* 275 (2008) 2221–2229, doi:[10.1098/rspb.2008.0531](https://doi.org/10.1098/rspb.2008.0531).
- [46] H. dos Santos Abreu, A.M. do Nascimento, M.A. Maria, Lignin structure and wood properties, *Wood Fiber Sci* 31 (1999) 426–433.
- [47] Q. Liu, L. Luo, L. Zheng, Lignins: biosynthesis and biological functions in plants, *Int. J. Mol. Sci.* 19 (2018), doi:[10.3390/ijms19020335](https://doi.org/10.3390/ijms19020335).
- [48] M.C. Jarvis, S.P.H. Briggs, J.P. Knox, Intercellular adhesion and cell separation in plants, *Plant. Cell Environ.* 26 (2003) 977–989, doi:[10.1046/j.1365-3040.2003.01034.x](https://doi.org/10.1046/j.1365-3040.2003.01034.x).
- [49] L.J. Gibson, *The hierarchical structure and mechanics of plant materials*, *J. R. Soc. Interface.* 9 (2012) 2749–2766.
- [50] W.G.T. Willats, L. McCartney, W. Mackie, J.P. Knox, Pectin: cell biology and prospects for functional analysis, *Plant Mol. Biol.* 47 (2001) 9–27, doi:[10.1023/A:1010662911148](https://doi.org/10.1023/A:1010662911148).
- [51] L.A. Baez, T. Tichá, T. Hamann, Cell wall integrity regulation across plant species, *Plant Mol. Biol.* 109 (2022) 483–504, doi:[10.1007/s11103-022-01284-7](https://doi.org/10.1007/s11103-022-01284-7).
- [52] V. Keryvin, M. Lan, A. Bourmaud, T. Parenteau, L. Charleux, C. Baley, Analysis of flax fibres viscoelastic behaviour at micro and nano scales, *Compos. Part A* 68 (2015) 219–225, doi:[10.1016/j.compositesa.2014.10.006](https://doi.org/10.1016/j.compositesa.2014.10.006).
- [53] J.J. Carruthers, A.P. Kettle, A.M. Robinson, Energy absorption capability and crashworthiness of composite material structures: a review, *Appl. Mech. Rev.* 51 (1998) 635–649, doi:[10.1115/1.3100758](https://doi.org/10.1115/1.3100758).
- [54] L. Zhang, Z. Bai, F. Bai, Crashworthiness design for bio-inspired multi-cell tubes with quadrilateral, hexagonal and octagonal sections, *Thin Walled Struct.* 122 (2018) 42–51, doi:[10.1016/j.tws.2017.10.010](https://doi.org/10.1016/j.tws.2017.10.010).
- [55] S. Bektas, *Intersection of an ellipsoid and a plane*, *Int. J. Res. Eng. Appl. Sci.* 6 (2016) 273–283.
- [56] L.T. Kuhn-Spearing, H. Kessler, E. Chateau, R. Ballarini, A.H. Heuer, S.M. Spearing, Fracture mechanisms of the *Strombus gigas* conch shell: implications for the design of brittle laminates, *J. Mater. Sci.* 31 (1996) 6583–6594, doi:[10.1007/BF00356266](https://doi.org/10.1007/BF00356266).